Nonlinear coupling effects of the thermocapillarity and insoluble surfactants to droplet migration under Poiseuille flow

Zhenlin Guo ⬡[*]

Mechanics Division, Beijing Computational Science Research Center, Beijing 100193, China

Under a fully developed Poiseuille flow with nonisothermal condition, it has been widely reported that the thermocapillary effects always strengthen the droplet migration velocity as long as the temperature increases along the direction of Poiseuille flow. The insoluble surfactant, on the other hand, always retards the droplet migration. This is due to the fact that, for most of the models, the Langmuir equation of state for the surface tension is usually simplified under the assumption of low surfactant concentration. The coupling term of temperature and surfactant concentration is dropped, and the thermo-induced and surfactant-induced Marangoni forces are therefore decoupled. In the present study, we develop a thermodynamically consistent phase-field model for investigating the coupling effects of temperature and surfactant concentration on droplet migration under a fully developed Poiseuille flow. By choosing the interface free energy sophisticatedly, the surface tension of our model consists of not only the classical linear part for the thermocapillary effects but also a nonlinear coupling term of temperature and surfactant concentration that recovers the Langmuir equation of state. This coupling term allows us to investigate the case of high surfactant concentration. Through 3D numerical simulations, we find that this nonlinear coupling term introduces extra thermo-induced and surfactant-induced Marangoni forces to the droplet migration, leading to a competition between the two, especially for the case of high surfactant concentration. In particular, the initial migration velocity of a surfactant-covered droplet is always faster than that of a droplet with a clean interface. The terminal velocity, on the other hand, does not reach its steady state but instead decreases gradually as the droplet moves toward the hotter region, whereas, for the case without this term, the initial migration velocity of a surfactant-covered droplet is always lower than that of a clean interface and the terminal velocity stays steady.

I. INTRODUCTION

The dynamics of droplets suspended in a pressure-driven flow has emerged one of the most important topics in science and engineering [1], as it has various applications in microfluidic devices, such as analytic detection [2], reagent mixing [3], drug delivery [4], and cell encapsulation processes [5]. The study of it has been the focus of research, both theoretical and experimental. Haber and Hetsroni [6] first solved the velocity solution of a deformed droplet with a clean interface under an imposed Poiseuille flow. Various extended works [7–13] are dedicated to investigating the

----

[*]zguo@csrc.ac.cn

nonlinear coupling effects, including the deformation, inertia, and fluid viscoelasticity to the droplet dynamics.

For most fluids, the surface tension generally decreases when the temperature increases. The variation of the temperature field across the droplet gives rise to the Marangoni force at the droplet interface, which induces droplet motion even in the absence of an imposed flow [14]. This effect is known as the thermocapillary effect and has important applications for droplet manipulation in a microchannel [15–17]. On the other hand, it is also a fundamental problem in the discipline of fluid mechanics. The pioneering work by Young *et al.* [14] derived an analytical expression for the migration velocity of a spherical drop in a quiescent liquid. Many subsequent works have been presented to investigate the more general cases, including the thermal convection, fluid inertia, and drop deformation that was neglected in [14,18–20]. Also the ambient flow condition is gradually released from a quiescent liquid to a uniform flow field and an unbounded Poiseuille flow in microchannels [21,22]. In summary, the thermocapillary effect has been known to have a significant influence on droplet migration.

Surfactants, as the surface-active agent, can also have considerable effects on droplet migration [23,24]. They are amphiphilic organic compounds, which not only can be absorbed at the droplet interface but also can migrate along the interface of a moving droplet. They thus tend to accumulate at the rear meniscus leading to a inhomogeneous local surfactant concentration at the interface, which produces gradients in surface tension and further gives rise to tangential forces along the interface. Through this Marangoni effect, surfactants can play an important role in droplet generation, droplet break-up, and coalescence, which are quite fundamental in microfluidic devices. Several works have been presented to study the dynamics of a surfactant-laden droplet under a Poiseuille flow [25–27], where the results show that the surfactant can not only retard the motion of droplet but also induce the cross-streamline migration of the drop towards the center of the Poiseuille flow.

As both the thermal- and surfactant-induced Marangoni effects have significant influences on the droplet motion under the Poiseuille flow, various works have been dedicated to investigating the coupling effects analytically and numerically [28–31]. For instance, Das *et al.* [28,29] studied the cross-stream migration of the droplet and obtained the droplet velocity analytically by neglecting the fluid inertia and thermal convection. Their results show that the motion of a surfactant-laden droplet in the combined presence of a temperature gradient and imposed Poiseuille flow cannot be obtained by a simple superposition of the following two independent results: migration of a surfactant-free droplet in a temperature gradient and the motion of a surfactant-laden droplet in a Poiseuille flow. Similarly, Sharanya *et al.* [30] have studied the motion of viscous surfactant-laden droplet in the combined presence of a temperature field and imposed Stokes flow. They show that the retardation due to the surfactants is marginal, and the thermal-induced Marangoni forces dominate the overall migration. Luo *et al.* [31] presented a three-dimensional numerical study on the thermocapillary migration of a surfactant-laden droplet under Poiseuille flow in a microchannel. Their result show that the surfactant-induced Marangoni forces always oppose the thermal-induced Marangoni force, and the competition between them is significantly altered by the convection. In all these works, however, the surfactant concentrations are assumed to be dilute or slightly higher, and the surface tension is simplified to be a linear function of the temperature and surfactant concentration, or a linear function with an extra simple product of temperature and surfactant concentration.

As pointed out by Luo *et al.* [31], the general case of nonlinear coupling variation of interfacial tension on both temperature and surfactant concentration in the case for the droplet migration has not been explored yet analytically and numerically, especially for the case of high surfactant concentration. Moreover, to our best knowledge, there is a lack of mathematical derivation for the interfacial flows coupling with thermocapillary effects and surfactants in a thermodynamically consistent framework. The objective of this paper is twofold: First, we aim to develop a thermodynamically consistent model with an easily implemented numerical tool to deal with the coupling of the surfactants and temperature field as well as the hydrodynamic flows. Second, we aim to

explore the effects of nonlinear coupling variation of surface tension on both temperature and surfactant concentration gradients to the droplet migration, especially for the case of high surfactant concentration.

From a numerical point of view, solving the problem of multiphase flows with soluble and insoluble surfactants and thermocapillary effects is highly challenging. The fluid-fluid interface is dynamic and complex, which may stretch, break up, or even coalesce with other interfaces. The heat equation and the bulk and interface surfactant system (PDEs) must be coupled with the fluid flows and solved on the moving, complex domain or interface. The available numerical methods for solving these problems can roughly be divided into two categories: interface-tracking and interface-capturing methods. Interface-tracking methods use either a separate grid for the interface or a set of interconnected points to mark the interface. In the context of the evolution of surfactant, examples are the boundary integral method (see [32] as the method review and [33–35] as examples), front-tracking method (see [36] as the review and [37,38] as examples), immersed boundary method (see [39] as the review and [40,41] as examples), and several hybrid methods [42–45]. In the context of the thermocapillary effects, we refer to [46] as a review. In general, interface-tracking methods can be made very accurate but can be relatively complicated to implement, especially in three dimensions and for problems involving interface topological changes.

In the interface-capturing methods, the interface is not tracked explicitly, but instead is implicitly defined through an auxiliary function (e.g., level-set, color, or phase-field function). This means that the solution of the problem can be done independently of the underlying grid, which greatly simplifies gridding, discretization, and handling of topological changes. In the context of the surfactant, examples are the level-set method (see [47] as the review and [48,49] as the examples), volume-of-fluid (VOF) method (see [50] as the review and [51,52] as the examples), and arbitrary Lagrangian-Eulerian (ALE) method (see [53] as the review and [54,55] as the examples).

Another interface capturing method is the phase-field method, which has now emerged as a powerful approach for simulating various types of multiphase flows [46,56,57]. The basic idea of the phase-field method is to treat the multiphase fluid as one fluid with variable material properties. An order parameter is employed to characterize the different phases, which varies continuously over thin interfacial layers and is mostly uniform in the bulk phases. Sharp interfaces are then replaced by thin but non-zero-thickness transition regions, where the interfacial forces are smoothly distributed. One set of governing equations for the mixture can be derived variationally from its energy density field, where the order parameter fields satisfy an advection-diffusion equation (usually the advective Cahn-Hilliard equations) and are coupled with Navier-Stokes equations through extra reactive stresses that mimic surface tension force.

Several phase-field models have been developed to simulate the two-phase flows with thermocapillary effects. In [46] the temperature field is introduced into the internal energy, free energy, and entropy leading to a temperature dependent surface tension for the thermocapillary effects. The phase-field model is then derived within a thermodynamically consistent framework such that the model equations satisfy the conservation of mass, momentum, energy, and entropy, which meanwhile allows for the fluid components to have different physical properties. The current work is also based on this framework.

A phase-field method has also been used for simulating the two-phase flows with surfactants [58–60]. In these models, another phase variable is employed to represent the bulk-interface surfactant concentrations simultaneously, and additional terms are introduced to the original Ginzburg-Landau free energy which account for the surfactant effects, including absorption, desorption, and the lowering of the surface tension. The model consists of Navier-Stokes equations governing the two-phase flows and two Cahn-Hilliard equations governing the fluid-fluid interface and the surfactant concentration, respectively. A similar idea is applied by Zhu *et al.* [60] to simulate a two-phase flow with soluble surfactant and moving contact line, where the model was obtained in a thermodynamically consistent way, such that the model equations satisfy the conservation of mass and energy. In this type of model, as the bulk-interface surfactant concentrations are now represented by one phase variable, only one equation governs the transportation of the

surfactant in the bulk and on the fluid-fluid interface simultaneously, whereas in the current work, our model is based on the sharp-interface surfactant equations, such that the bulk-interface surfactant equations are computed separately.

Since the phase variable is introduced to characterize the different regions and the interface, it can be further used to solve partial differential equations in or on a complex domain or interface. This is the so-called diffuse-domain method [61–65]. In the diffuse-domain method, we can extend any dynamic and complex domain or interface to a larger and regular domain, and use a phase variable to smoothly approximate the characteristic function of the original domain or interface. The original partial differential equation is then reformulated on the larger domain with additional source terms that approximate the boundary conditions. It has been shown that the reformulated partial differential equation asymptotically converges to the original system as the width of the diffuse interface layer tends to zero [63]. The advantages of such a method are that no modifications of standard software packages are required and the stationary or moving complex boundary can be imposed easily and smoothly.

In [61] a phase-field method is coupled with the diffuse-domain method to simulate the two-phase flow problem with a soluble surfactant, where the fluid-fluid interfaces are represented implicitly by a phase variable. The bulk (interface) surfactant equations are then coupled with the phase variable (a delta function based on the phase variable) and extended on a larger and regular domain, where the additional terms are introduced as source terms to the bulk-interface surfactant equations approximating the adsorption-desorption flux boundary conditions. However, since the equations of fluid flows and surfactants are simply coupled, the model does not satisfy the conservation of energy. Moreover, the model is restricted only to the matched density and isothermal case.

In the present paper, we develop a thermodynamically consistent phase-field model for two-phase flows with thermocapillarity and insoluble surfactant. We apply the phase-field method for modeling the two-phase flows with thermocapillary effects, and use the diffuse-domain method for coupling the two-phase flows with a sharp-interface surfactant equation. The model consists of Navier-Stokes equations for the fluid flows, a Cahn-Hilliard equation for the fluid-fluid interface, a heat equation, and the bulk-interface surfactant equations in the diffuse-domain formulation. Our model allows for the binary incompressible fluid to have different densities, viscosities, and thermal conductivities for each component, which meanwhile maintains the conservation of mass, momentum, energy and entropy. In addition, the interface free energy is chosen sophisticatedly, leading to a surface tension that consists of not only a classical linear part for the thermocapillary effects but also a nonlinear coupling term of temperature and surfactant concentration that covers the classical Langmuir equation of state for surface tension.

Our paper is organized as follows: we first present the model derivations in Sec. A and then discuss the problem setup and the nondimensionalization in Sec. II. We validate our model and numerical methods through several tests and benchmarks in Sec. III. Finally, we show the numerical results in Sec. IV and conclude in Sec. V. The Appendixes show the details of model derivations.

II. PROBLEM SETUP AND NONDIMENSIONALIZATION

A. Problem setup

In this study we consider the motion of a surfactant-covered droplet in a square microchannel under a fully developed Poiseuille flow with a linearly increasing temperature field imposed along the flow direction, where the temperature gradient is a constant $\partial T / \partial z = \nabla T_\infty$. See Fig. 1 as an illustration for the problem setup. The size of the square microchannel is $[-H, H] \times [-H, H] \times [0, 8H]$, where the fluid flows upwards along z axis. The droplet (fluid 2) of radius R^* is initially centered at $(0, 0, 1.5R^*)$ and is surrounded by another immiscible fluid (fluid 1) in the square microchannel. Here we investigate only the behavior of droplets moving along the microchannel centerline z axis; therefore, there is no cross-stream droplet migration taking place, i.e., the droplet velocities in the direction of the x and y axes are always zero due to the symmetry. The steady unidirectional flow
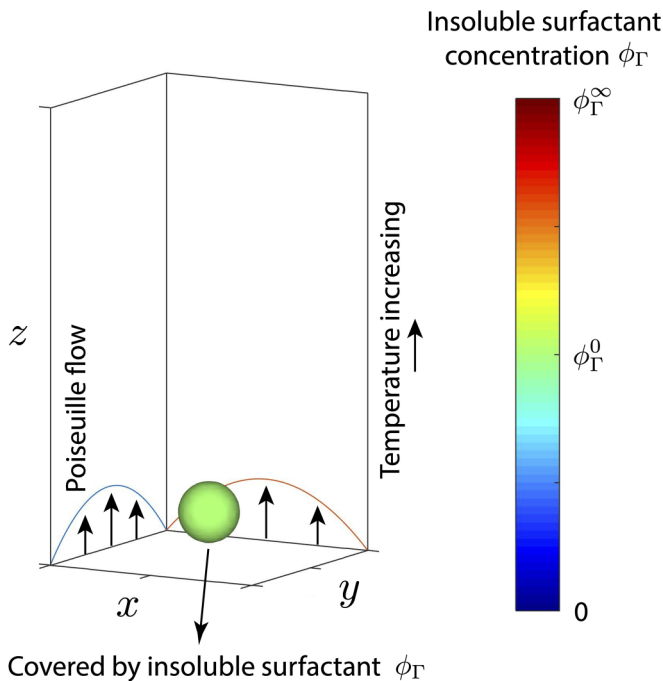
FIG. 1. Problem setup. A surfactant-covered droplet is initially centered at the centerline of a square microchannel under a fully developed Poiseuille flow. The initial temperature field is assumed to be linearly increasing along the flow direction (z axis).

(velocity component W in the direction of the z axis) in the square microchannel far from the droplet is given by [66]

$$W(x, y, z) = K(H^2 - y^2) + K \sum_{n=1}^{\infty} B_n \cosh{(\alpha_n x)} \cos{(\alpha_n y)}, \tag{1}$$

$$K = -\frac{dp/dz}{2\mu_1}, \quad B_n = \frac{(-1)^n 4H^2}{\alpha_n^3 \cosh{(\alpha_n)}}, \quad \alpha_n = \frac{(2n-1)\pi}{2}. \tag{2}$$

Here dp/dz is a constant pressure gradient along z axis that drives the fluid flow. The maximum velocity in the square microchannel can be given as $V^* = KH^2$. In our computations, we neglect terms with $n > 40$ in Eq. (2), which creates a truncation error on the order of 10^{-5}. Moreover, the droplet is initially covered by the insoluble surfactant with an initial concentration ϕ_Γ^0.

B. Nondimensionalization

In the present study, we applied a diffuse-interface based model for the numerical simulations. In particular, we applied the phase-field method for simulating the two-phase flows, which is coupled with the diffuse domain method for the insoluble surfactants on the fluid-fluid interface. The model derivations are done by following a thermodynamically consistent framework that ensures the conservation laws of the two-fluid system. The dimensional system equations and the corresponding derivations are presented in Appendix A. We now nondimensionalize the system based on the above setup. Using the properties of fluid 1 as the characteristic quantities, we nondimensionalize the variable properties as

$$\bar{\Lambda} = c + \zeta_\Lambda (1 - c), \tag{3}$$

where ζ_Λ are the corresponding physical property ratios. By choosing R^*, V^*, and $\nabla T_\infty R^*$ as the characteristic length, velocity, and temperature, $\mu_c^* = \rho_1(V^*)^2$ the characteristic chemical potential and pressure, ϕ_Γ^∞ the characteristic interface surfactant concentration, respectively, and m_c^* the characteristic mobility for the phase field, we nondimensionalize the physical quantities as follows:

$$\bar{t} = \frac{tV^*}{R^*}, \quad \bar{\boldsymbol{v}} = \frac{\boldsymbol{v}}{V^*}, \quad \bar{T} = \frac{T - T_0}{\nabla T_\infty R^*}, \quad \bar{\epsilon} = \frac{\epsilon}{R^*}, \quad \bar{m}_c = \frac{m_c}{m_c^*},$$

$$\bar{\phi}_\Gamma = \frac{\phi_\Gamma}{\phi_\Gamma^\infty}, \quad \bar{\mu}_c = \frac{\mu_c}{\rho_1(V^*)^2}, \quad \bar{p} = \frac{p}{\rho_1(V^*)^2}. \tag{4}$$

Note that the above setup is considered for all the computations in Sec. 5. It might be slightly modified in Sec. 4 for benchmark validations. We then nondimensionalize the surface tension defined in Eq. (A35) by using σ_0, such that

$$\bar{\sigma}_f(\bar{\phi}_\Gamma, \bar{T}) = \frac{1}{\sigma_0}\left[\sigma_0 + \frac{\partial \tilde{\sigma}_0}{\partial T}(T - T_0) + RT\phi_\Gamma^\infty \ln\left(1 - \frac{\phi_\Gamma}{\phi_\Gamma^\infty}\right)\right]$$

$$= 1 - \mathrm{Ca}[\mathrm{Ma}_T \bar{T} - \mathrm{Ma}_{\Gamma 1} \ln(1 - \bar{\phi}_\Gamma) - \mathrm{Ma}_{\Gamma 2} \bar{T} \ln(1 - \bar{\phi}_\Gamma)], \tag{5}$$

where

$$\mathrm{Ca} = \frac{\mu_1 V^*}{\sigma_0}, \quad \mathrm{Ma}_T = -\frac{\partial \tilde{\sigma}_0}{\partial T}\frac{\nabla T_\infty R^*}{\mu_1 V^*}, \quad \mathrm{Ma}_{\Gamma 1} = \frac{R\phi_\Gamma^\infty T_0}{\mu_1 V^*}, \quad \mathrm{Ma}_{\Gamma 2} = \frac{R\phi_\Gamma^\infty \nabla T_\infty R^*}{\mu_1 V^*}. \tag{6}$$

Here Ca is the capillary number, and Ma_T is the thermal Marangoni number representing the relative strength of thermal-induced interface-tension-driven Marangoni flow and the imposed Poiseuille flow. In addition, we introduce two surfactant Marangoni numbers $\mathrm{Ma}_{\Gamma 1}$ and $\mathrm{Ma}_{\Gamma 2}$ that measure the relative strength of surfactant-induced interfacial-tension-driven Marangoni flow to that of the imposed Poiseuille flow with respect to the reference temperature T_0 and the temperature difference across the droplet $\nabla T_\infty R^*$, respectively. Moreover, Bi and all the other nondimensional parameters are given by

$$\mathrm{Bi} = \frac{r^d R^*}{\phi_\Gamma^\infty V^*}, \quad \mathrm{Re} = \frac{\rho_1 V^* R^*}{\mu_1}, \quad \mathrm{Pe}_T = \frac{\rho_1 c_{hc1}^* V^* R^*}{k_1}, \quad \mathrm{Pe}_c = \frac{V^* R^*}{m_c^* \mu^*}, \quad \mathrm{Pe}_\Gamma = \frac{V^* R^*}{m_{\phi_\Gamma}},$$

$$\mathrm{Pe}_i = \frac{V^* R^*}{m_{\phi_i}}, \quad \mathrm{Ec} = \frac{(V^*)^2}{c_{hc}^* T^*}, \quad \mathrm{M}_\Gamma = \frac{\rho_1(V^*)^2}{(\phi_\Gamma^\infty)^2 R^*}, \quad \mathrm{We} = \mathrm{Ca}\,\mathrm{Re}, \quad \mathrm{El} = \mathrm{Ca}\,\mathrm{Ma}_{\Gamma 1}, \tag{7}$$

where Bi is the Biot number, Re is the Reynolds number, Pe_T, Pe_c, Pe_Γ are the Péclet numbers for the heat equation, phase field, and interface surfactants, respectively, Ec is the Eckert number, and M_Γ is the Mach number for the interface surfactants, respectively, We is the Weber number, and El is the elastic number. After dropping the bar notations, the nondimensional phase-field model for two-phase flows with thermocapillary effects and insoluble surfactants can be given as follows:

$$\rho \boldsymbol{v}_t + \rho \boldsymbol{v} \cdot \nabla \boldsymbol{v} = \nabla \cdot \mathbf{m}, \tag{8}$$

$$\nabla \cdot \boldsymbol{v} = \frac{\alpha}{\mathrm{Pe}_c} \nabla \cdot (m_c \nabla \mu_c), \tag{9}$$

$$c_t + \nabla \cdot (\boldsymbol{v}c) = \frac{1}{\mathrm{Pe}_c} \nabla \cdot (m_c \nabla \mu_c), \tag{10}$$

$$(\delta \phi_\Gamma)_t + \nabla \cdot (\boldsymbol{v}\delta\phi_\Gamma) = \frac{1}{\mathrm{Pe}_\Gamma} \nabla \cdot (\delta \nabla \phi_\Gamma), \tag{11}$$

$$(\rho c_{hc} T)_t + \nabla \cdot (\boldsymbol{v}\rho c_{hc} T) = \frac{1}{\mathrm{Pe}_T} \nabla \cdot (k\nabla T) + \mathrm{Ec}\, h_s, \tag{12}$$

where

$$\mathbf{m} = \frac{1}{\text{We}}\sigma_f(\phi_\Gamma, T)[\delta\mathbf{I} - \eta\epsilon(\nabla c \otimes \nabla c)] - p\mathbf{I} + \frac{1}{\text{Re}}\boldsymbol{\tau} - \tilde{p}\mathbf{I}, \tag{13}$$

$$\sigma_f(\phi_\Gamma, T) = 1 - \text{Ca}[\text{Ma}_T T - \text{Ma}_{\Gamma 1}\ln(1 - \phi_\Gamma) - \text{Ma}_{\Gamma 2} T \ln(1 - \phi_\Gamma)], \tag{14}$$

$$\boldsymbol{\tau} = \mu(\nabla\boldsymbol{v} + \nabla\boldsymbol{v}^T) - \frac{2}{3}\mu(\nabla\cdot\boldsymbol{v})\mathbf{I}, \tag{15}$$

$$\mu_c = \frac{\eta}{\text{We}}\mu_0 + \alpha p, \tag{16}$$

$$\mu_0 = h'(c) - \epsilon\Delta c. \tag{17}$$

Here the nondimensional terms $\tilde{p}$ and h_s are given in D 1. Choosing $\rho_1(V^*)^2$ as the characteristic energy density, the nondimensional internal energy and free energy densities are given by

$$\hat{u} = \frac{1}{\text{Ec}}\rho c_{hc}T + \frac{1}{\text{We}}\delta\gamma_u(\phi_\Gamma), \tag{18}$$

$$\hat{f} = \frac{1}{\text{Ec}}\rho c_{hc}T - \frac{1}{\text{Ec}}\rho c_{hc}T\ln\left(\frac{T}{T_0}\right) + \frac{1}{\text{We}}\delta\gamma_f(\phi_\Gamma, T). \tag{19}$$

After the nondimensionalization, we consider a square microchannel of $[-h, h] \times [-h, h] \times [0, 8h]$ with $h = H/R^*$, in which a droplet of radius 1 is initially centered at (0,0,1.5). The following initial conditions are imposed:

$$u(x, y, z, 0) = 0, \tag{20}$$

$$v(x, y, z, 0) = 0, \tag{21}$$

$$w(x, y, z, 0) = W/V^*, \tag{22}$$

$$T(x, y, z, 0) = z, \tag{23}$$

$$\phi_\Gamma(x, y, z, 0) = \phi_\Gamma^0, \tag{24}$$

$$c(x, y, z, 0) = 0.5 + 0.5\tanh\left[(1 - r)/2\sqrt{2}\epsilon\right], \tag{25}$$

where W is defined by Eq. (1) with $K = 1$, $r = \sqrt{x^2 + y^2 + (z - 1.5)^2}$ and ϕ_Γ^0 is a constant that will be specified later.

On all the side boundaries ($x = \pm h$ or $y = \pm h$), we apply no-slip boundary conditions (BCs) for the velocity $\boldsymbol{v}$, and fix the temperature as $T = z$. On the top and bottom boundaries ($z = 0, 8h$), we fix $\boldsymbol{v}$ and T by using Eqs. (20)–(23). Moreover, no-flux BCs are imposed for c, μ_c, and ϕ_Γ on all the boundaries.

Due to the appearance of the nonlinear coupling term in the surface tension (14), the model allows us to investigate the case with insoluble surfactant in high concentration. Moreover, by calculating the derivatives of surface tension, we obtain the thermal-induced and surfactant-induced Marangoni forces, respectively:

$$\frac{\partial\sigma_f(\phi_\Gamma, T)}{\partial T} = -\text{Ca}\,\text{Ma}_T + \text{Ca}\,\text{Ma}_{\Gamma 2}\ln(1 - \phi_\Gamma), \tag{26}$$

$$\frac{\partial\sigma_f(\phi_\Gamma, T)}{\partial\phi_\Gamma} = -\text{Ca}\,\text{Ma}_{\Gamma 1}\frac{1}{1 - \phi_\Gamma} - \text{Ca}\,\text{Ma}_{\Gamma 2}T\frac{1}{1 - \phi_\Gamma}. \tag{27}$$

From Eq. (26), we observe that for the case with high surfactant concentration, as ϕ_Γ approaches 1 (or, say, ϕ_Γ^∞), the temperature derivative becomes strongly negative, indicating that the surface

tension becomes increasingly sensitive to the temperature field at the evaluated surfactant concentration. Meanwhile, the surfactant concentration derivative (27) also becomes strongly negative, where the magnitude becomes even larger as T increases. Therefore, higher surfactant concentration would lead to a stronger competition between the thermal-induced and surfactant-induced Marangoni forces, which is significantly affected by both the temperature and surfactant concentration. See Sec. IV B for the numerical investigation and discussion.

Note that for the case with dilute surfactant concentration where ϕ_Γ is small, we can simplify the surface tension Eq. (14) to obtain

$$\sigma_f(\phi_\Gamma, T) = 1 - \mathrm{Ca}\,\mathrm{Ma}_T T - \mathrm{Ca}\,\mathrm{Ma}_\Gamma \phi_\Gamma, \tag{28}$$

where the surface tension is assumed to be linearly depending on both the temperature and interface surfactant concentration, the logarithm is simplified to be a linear function of ϕ_Γ, and the coupling term is dropped. Here $\mathrm{Ma}_\Gamma = \mathrm{Ma}_{\Gamma 1}$ as defined in Eq. (7). This simplification is commonly performed for the convenience of the mathematical calculations and is valid only for dilute concentration case. Same or similar simplified formulations for surface tension can be found in [28–31], where the cases with dilute surfactant concentrations are considered. It can be observed clearly that the thermo- and surfactant-induced Marangoni forces are decoupled after this simplification, and the coupling effects are ignored.

III. NUMERICAL VALIDATIONS

In this section we present several numerical tests to validate our nondimensional model (8)–(12) and the corresponding numerical method. A semi-implicit, staggered finite difference numerical method developed in [67] is applied here for the computations. A block-structured, adaptive multigrid (BSAM) solver [67,68] is used for the implementations.

A. Thermocapillary migration of deformable droplet with infinitely small Pe_T and clean interface

Thermocapillary migration of droplets was first analyzed by Young *et al.* [14] for the flows with infinitesimal Marangoni number, in which the convective transport of energy can be neglected compared to molecular transport of these quantities. The governing equations can therefore be linearized. The dimensional terminal migration velocity (also known as YGB velocity) of a spherical droplet with radius R in a constant temperature gradient ∇T_∞ within an unbounded fluid medium can be given as

$$V_{YGB} = -\frac{\partial \tilde{\sigma}_0}{\partial T} \frac{2R\,\nabla T_\infty}{6\mu_1 + 9\mu_2}. \tag{29}$$

Note that as there is no base flow imposed in the square microchannel, we choose V_{YGB} as the characteristic velocity for the nondimensionalization. All the other scaling and settings are the same as in Sec. II B. For the computations, we consider a square microchannel with $h = 4$. We fix the temperature field as its initial condition and ignore the surfactants by treating the concentration ϕ_Γ as zero. In addition, we assume that the surface tension is only a linear function of temperature, such that

$$\sigma_f(T) = 1 - \mathrm{Ca}\,\mathrm{Ma}_T T. \tag{30}$$

On all the boundaries, no-slip BCs are imposed for the velocity $\boldsymbol{v}$, and no-flux BCs are imposed for the phase-field functions c and μ_c. The physical property ratios and the corresponding nondimensional parameters are given as

$$\zeta_\rho = 2, \quad \zeta_\mu = 0.1, \quad \mathrm{Ma}_T = 0.2899, \quad \mathrm{Re} = 1, \quad \mathrm{Ca} = 0.2, \quad \mathrm{Pe}_c = \epsilon/10. \tag{31}$$

To compare the numerical results with the analytical solution V_{YGB}, we calculate the migration velocity V_R of the droplet after every time step with $V_R = \int_\Omega c\boldsymbol{v} \cdot \hat{\boldsymbol{z}}\, dV / \int_\Omega c\, dV$. As the
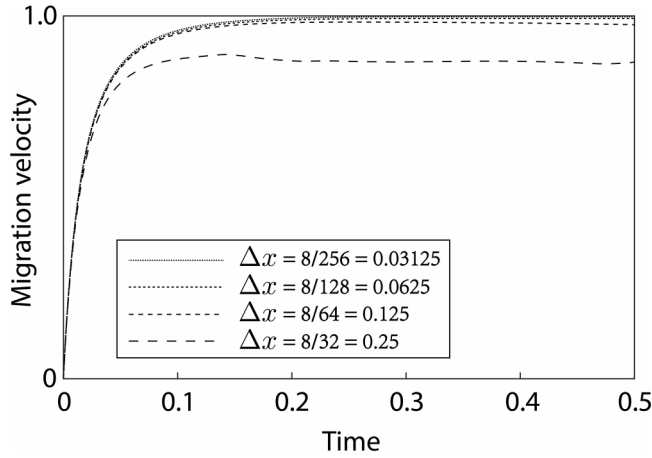
FIG. 2. Thermocapillary migration velocity of a droplet induced by a linearly increasing temperature field along the microchannel. The dotted lines are the nondimensional migration velocities V_R with various spacing size ($\Delta x = 8/n$ with $n = 32, 64, 128, 256$) and a fixed $\epsilon = 0.03$.

thermocapillary migration is driven by the surface tension gradient, the diffuse interface needs to be resolved carefully. We first test the convergence of the results by refining the spacing size Δx with a fixed ϵ. In particular, we set $\epsilon = 0.03$ and use four spacing sizes $\Delta x = 8/n$ for the computations, where $n = 2^{(4+k)}$ with $k = 1, 2, 3, 4$, respectively. The numerical results are shown in Fig. 2, where we can see that the migration velocity seems to converge when $n = 2^7$ and $n = 2^8$. We then show the convergence of the model by testing four values of $\epsilon (= 0.03, 0.06, 0.12, 0.24)$ with a fixed grid size $n = 2^7$. The numerical results are shown in Fig. 3, where we observe that after an initial acceleration phase, the migration velocity approaches the theoretical prediction of sharp-interface model, V_{YGB}, asymptotically. Based on these results, we choose $n = 2^7$ and $\epsilon = 0.03$ for all the computations in Sec. 5.
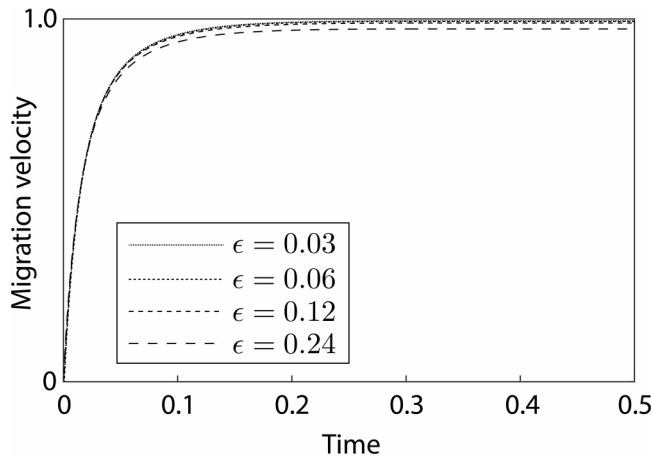

FIG. 3. Thermocapillary migration velocity of a droplet induced by a linearly increasing temperature field along the microchannel. The dotted lines are the nondimensional migration velocities V_R with various ϵ and a fixed grid size $n = 128$.
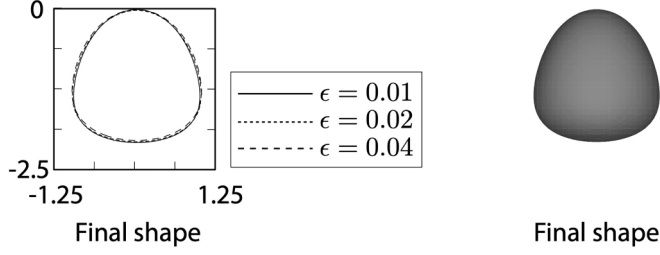
FIG. 4. The deformation of a droplet with clean interface in the square microchannel under a fully developed Poiseuille flow with the isothermal condition. Left: Steady-state droplet profiles at the plane $y = 0$ with various ϵ. Right: The corresponding droplet surface for $\epsilon = 0.01$. The capillary number is Ca $= 0.1$ and viscosity ratio is $\zeta_v = 2.04$.

B. Droplet motion in a square microchannel with clean interface under isothermal condition

We next validate our numerical method for simulating the motion of a droplet with clean interface in a square microchannel under a fully developed Poiseuille flow, where the isothermal condition is considered. The setup is the same as mentioned in Sec. II B except that a longer square domain of size $[-1.25, 1.25] \times [-1.25, 1.25] \times [0, 10]$ is considered. The droplet of radius 1 is initially located at (0,0,1.5). The two fluids are of the following property ratios:

$$\zeta_\rho = 1, \quad \zeta_\mu = 2.04. \tag{32}$$

As the isothermal condition is considered, and there is no surfactant, the surface tension is assumed to be constant over the droplet interface. Here to compare with the existing benchmark results, the deformation D for a droplet moving along the microchannel centerline is defined as the ratio of the droplet length l_z along the z axis to the droplet length l_x along the x axis, such that $D = l_z/l_x$.

We first carry out a convergence test by refining ϵ with a fixed grid size n. In particular, we set the grid size $[n \times n \times 4n]$ with $n = 2^7$ with $\epsilon = 0.04, 0.02,$ and 0.01, respectively. In Fig. 4 we show the final droplet shapes at the plane $y = 0$, where it can be observed that the droplet interfaces seem to converge as we refine ϵ.
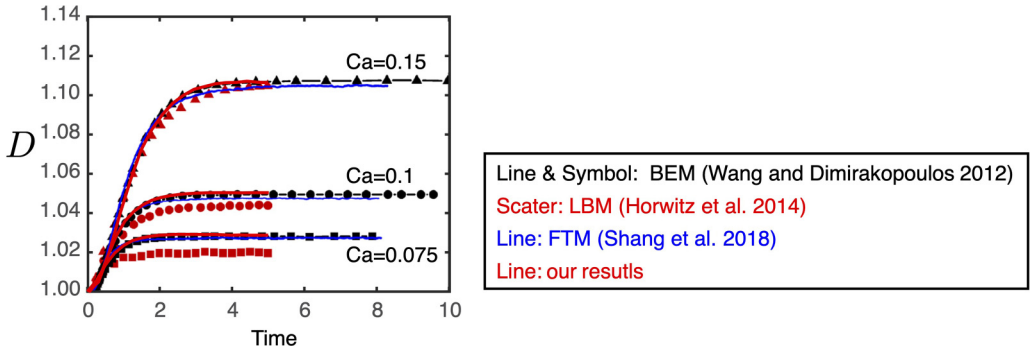
FIG. 5. Time evolution of droplet deformation D with size $r = 0.8$ moving in a square microchannel under a fully developed Poiseuille flow. Our results are compared with several existing numerical studies with various capillary number Ca $= 0.075, 0.1, 0.15$ and a fixed viscosity ratio $\zeta_\mu = 2.04$. The black lines with symbols denote the results obtained by using the boundary element method (BEM) [69], the scattered red lines denote the result by the lattice Boltzmann method (LBM) [70], the blue solid lines denote the result by the front-tracking method (FTM) [71], and the red solid lines denote our result.

In Fig. 5 the time evolutions of droplet deformation are presented for various capillary numbers Ca$(= 0.075, 0.1, 0.15)$ with a fixed $\epsilon = 0.01$. Quantitative comparisons are given between our results and those of previous studies, including the boundary element method (BEM) [69], kattice Boltzmann method (LBM) [70], and front-tracking method (FTM) [71]. As the droplet is suddenly released at the centerline of the square microchannel under a fully developed Poiseuille flow, it starts to elongate along the flow direction. Eventually, the drop shape reaches a steady state and shows no change any longer. Excellent agreement is observed between our predictions and other works on both transient and steady-state values of the drop deformation.

C. Interface surfactant diffusion on a stationary or moving circle

Finally, we consider the interface surfactant diffusion on a stationary and a moving circle. This tests the validity of the diffuse-domain representation of the interface (11), and the corresponding diffusion term.

We first consider a stationary circle of radius 1, with an initial interface surfactant concentration given by

$$\phi_\Gamma(\theta, t = 0) = \tfrac{1}{2}[1 - \cos(\theta)], \tag{33}$$

where θ denotes the angle measured in the counterclockwise direction from the negative part of y axis. The interface surfactant concentration equation can now be written in polar coordinates as

$$\frac{\partial \phi_\Gamma(\theta, t)}{\partial t} = \frac{1}{\mathrm{Pe}_\Gamma R^2} \frac{\partial^2 \phi_\Gamma(\theta, t)}{\partial \theta^2}, \tag{34}$$

with the initial condition (33) and periodic boundary condition in the θ direction. Solving Eq. (34), we obtain

$$\phi_\Gamma(\theta, t) = \frac{1}{2}\left[1 - \exp\left(-\frac{t}{\mathrm{Pe}_\Gamma R^2}\right) \cos \theta\right]. \tag{35}$$

For the simulations, we consider a two-dimensional computational domain $[-2, 2] \times [-2, 2]$ with a circle of radius 1 placed in the center of the domain. The initial conditions for the interface surfactant concentration ϕ_Γ and the phase-field variable c are given by Eq. (33) and the following, respectively:

$$c(x, y, t = 0) = \frac{1}{2}\left(1 + \tanh \frac{1 - \sqrt{x^2 + y^2}}{2\sqrt{2}\epsilon}\right). \tag{36}$$

To enable a direct comparison with the analytical solution, the surfactant concentration at the interface is needed. In the present study, a staggered finite difference method is used for computations in the present study, where the phase variable c and the interface surfactant concentration ϕ_Γ are defined at the cell center. The fluid-fluid interface $\Gamma(t)$, on the other hand, is represented by the contour $c = 0.5$, which may not be on the cell center exactly. We first apply a marching squares algorithm [61] to generate a set of points on the contour $c = 0.5$. We then use bilinear interpolation to interpolate the grid values of ϕ_Γ to these interface points, and finally compare with those of the analytical solutions. Note that this will introduce extra uncertainties, so the absolute errors given later may not be exact values. However, the order of convergence results should not be affected by this.

Figure 6 shows the comparisons between the numerical solution and the analytical solution with various Pe_Γ at different times. Good agreement is observed. The error in the infinity norm between the interpolated values and the exact values on the interface is given in Table I. The numerical solution converges towards the exact solution in a second-order fashion.

We next consider the interface surfactant diffusion on a moving circle, where we set a constant velocity field $\boldsymbol{v} = (2, 2)$. The analytical solution is the same, only translated in the computational domain. The new computational domain is $[-2, 4] \times [-2, 4]$, which is extended to accommodate the translation. Again, the circle of radius 1 is initially located at $[0,0]$.
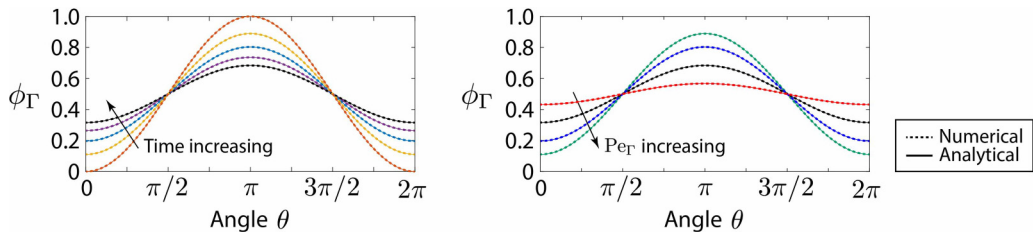
FIG. 6. Comparisons of the numerical results (dotted colorful lines) and exact solutions (solid colorful lines) for the interface surfactant concentration diffusion on a stationary circle in Sec. III C. The grid spacing is $h = 1/128$ with $\epsilon = 0.0125$. Left: ϕ_Γ profiles at times $t = 0.0,\ 0.25,\ 0.5,\ 0.75$, and 1.0 for $\mathrm{Pe}_\Gamma = 1$. Right: ϕ_Γ profiles at time $t = 1.0$ for $\mathrm{Pe}_\Gamma = 0.5,\ 1,\ 2$, and 4.

The initial and final interface surfactant concentrations are given in Fig. 7. As shown in Table II, the convergence rate is also second order as in the diffusion only test case. However, the errors are slightly higher due to the additional errors caused by the advection. Note that the accuracy order with respect to ϵ of our diffuse domain method will be presented in a separate paper, where several diffuse domain interface representations will be investigated through asymptotic analysis and numerical simulations.

IV. COUPLING EFFECTS OF THERMOCAPILLARITY AND INSOLUBLE SURFACTANTS

We now investigate the nonlinear coupling effects of thermocapillarity and insoluble surfactants on the droplet migration in a square microchannel under a fully developed Poiseuille flow. All the settings are described in Sec. II B. Here we set $h = 4$ for the square microchannel domain. The droplet (fluid 2) is surrounded by another immiscible fluid (fluid 1) with the following physical property ratios:

$$\zeta_\rho = 1.89, \quad \zeta_\mu = 0.14, \quad \zeta_k = 0.47, \quad \zeta_{hc} = 0.69. \tag{37}$$

Moreover, for the base case, we set the parameters as follows:

$$\mathrm{Re} = 2, \quad \mathrm{Ca} = 0.1, \quad \mathrm{Pe}_c = \epsilon/10, \quad \mathrm{Ec} = 1, \quad \mathrm{M}_\Gamma = 1,$$
$$\mathrm{Pe}_T = 5, \quad \mathrm{Ma}_T = 0.1, \quad \mathrm{Ma}_{\Gamma 1} = 0.5, \quad \mathrm{Ma}_{\Gamma 2} = 0.1. \tag{38}$$

Note that the above setup is relevant to a system of Fluorinert FC-75 droplet in silicone oil in a (millimetric) microchannel [72,73]. The dimensional parameters can be set as $R = 8.13$ (J K^{-1} mol^{-1}), $\phi_\Gamma^\infty = 8.856 \times 10^{-4}$ (mol m^{-2}), $T_0 = 300$ (K), $\mu_1 = 864$ (N s m^{-2}), $\nabla T_\infty = 10^4$ (K m^{-1}), $R^* = 0.6 \times 10^{-2}$ (m), $V^* = 5 \times 10^{-3}$ (m s^{-1}), and $\sigma_T = 0.036$ (N m^{-1} K^{-1}). Here we refer to [72,73] for more details about the dimensional parameters and setup.

TABLE I. Convergence test for the interface surfactant diffusion on a stationary circle at $t = 1$ in Sec. III C.

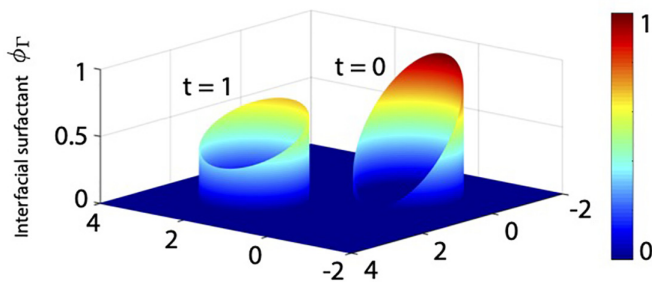| ϵ	h	Error in L_∞	Order
0.2	1/8	1.44×10^{-2}	—
0.1	1/16	4.62×10^{-3}	1.64
0.05	1/32	1.10×10^{-3}	2.07
0.025	1/64	2.05×10^{-4}	2.42
0.0125	1/128	4.03×10^{-5}	2.35

FIG. 7. Interface surfactant concentration ϕ_Γ on a moving circle at time $t = 0$ (right) and $t = 1$ (left). The grid spacing is $h = 1/128$ with $\epsilon = 0.0125$.

A. Thermocapillary migration of a clean droplet in a microchannel under Poiseuille flow

We first investigate how the thermal convection affects the thermocapillary migration of a clean droplet in the microchannel under a fully developed Poiseuille flow. In Fig. 8 we show the effects of thermal Péclet number Pe_T to the migration velocity. As can be observed all the droplets under the nonisothermal condition are migrating faster than the droplet under the isothermal condition. This is due to the thermal-induced Marangoni force that drags the droplet moving toward the hotter region. Moreover, as we increase Pe_T, the terminal droplet migration velocity decreases. This is due to the fact that the corresponding isothermal contours (see Fig. 9) become more densely distributed, which gives rise to smaller temperature gradients along the droplet interface and therefore a smaller thermal-induced Marangoni force.

B. Surfactant-covered droplet under Poiseuille flow

We next investigate the nonlinear coupling effects of the thermocapillarity and insoluble surfactants.

1. Effects of the initial surfactant concentration ϕ_Γ^0

We first test the effects of the initial interface surfactant concentration ϕ_Γ^0 on the droplet migration velocity. Two cases, one without the nonlinear coupling term ($\mathrm{Ma}_{\Gamma 2} = 0$) and the other one with it ($\mathrm{Ma}_{\Gamma 2} = 0.1$) in the surface tension formula (14), are compared. As can be observed from Fig. 10(a), the droplets with clean interface under nonisothermal condition achieves the largest terminal velocity for both cases. This is followed by the droplets covered by insoluble surfactants where the terminal velocity decreases as ϕ_Γ^0 increases. The droplet with a clean interface under an isothermal condition achieves the smallest terminal velocity. Figures 10(c)–10(e) present the interface surfactant concentration, temperature, and surface tension, respectively, for both cases at time $t = 20$. These quantities are plotted along the droplet interface as functions of angle θ on the 2D plane $(x, y = 0, z)$, where θ is measured anticlockwise while treating the droplet center as the

TABLE II. Convergence test for the interface surfactant diffusion on a moving circle at $t = 1$ in Sec. III C.

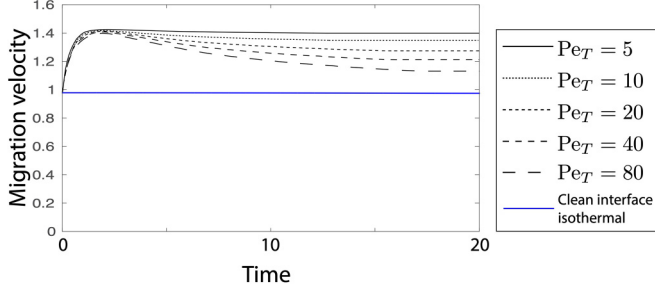| ϵ	h	Error in L_∞	Order
0.2	1/8	1.50×10^{-2}	—
0.1	1/16	5.30×10^{-3}	1.64
0.05	1/32	2.00×10^{-3}	2.07
0.025	1/64	4.45×10^{-4}	2.42
0.0125	1/128	4.03×10^{-5}	2.35

FIG. 8. Evolution of migration velocities for droplets under a fully developed Poiseuille flow with non-isothermal condition of various Pe_T (black lines) and isothermal condition (solid blue). A linearly increasing temperature field is initially imposed along the flow direction for the nonisothermal case.

origin with $\theta = \pi/2$ representing the droplet front and $\theta = 3\pi/2$ for the droplet rear. For the sake of simplicity, we show these quantities by subtracting their mean values over the droplet interface.

It can be observed that the thermal-induced Marangoni force accelerates the droplet migration while the surfactant retards the migration, which indicates that the surfactant-induced Marangoni force always opposes the thermal-induced Marangoni force. Although the retardation becomes stronger as we increase ϕ_Γ^0, the thermal-induced Marangoni force always dominates the surfactant-induced Marangoni force. In addition, the surfactant introduces stabilization effect for both cases, where as long as the droplet is covered by surfactant, the migration velocity would reach its (quasi) steady state faster than that of the droplet with clean interface. This stabilization effect becomes stronger as we increase ϕ_Γ^0.

Two other interesting scenarios can be observed while comparing the cases with and without the nonlinear coupling term. First, the nonlinear coupling term introduces an extra acceleration effect to the droplet migration at an early stage. As can be observed from Fig. 10(b), when the nonlinear coupling term appears ($Ma_{\Gamma 2} = 0.1$) in the surface tension, all the velocities of droplets covered by surfactants are initially larger than that of the droplet with a clean interface. In addition, the initial acceleration effects become stronger as we increase ϕ_Γ^0. As discussed under Eqs. (26) and (27), with a larger ϕ_Γ^0, the surface tension becomes more sensitive to the temperature, leading to a stronger thermal-induced Marangoni force that accelerates the droplet at an early stage. On the other hand, when the nonlinear coupling term disappears ($Ma_{\Gamma 2} = 0$), the velocities of droplets covered by surfactants are always lower than that of the droplet with clean interface, which is due to the fact that the extra acceleration effects are missing, and the retardation is induced by the surfactant. Second, the terminal migration velocities slightly decrease for any $Ma_{\Gamma 2} > 0$ as time passes, whereas for $Ma_{\Gamma 2} = 0$, the terminal velocities stay steady. This is due to the effects of the nonlinear coupling term that is discussed under Eq. (27). As the droplet migrates upward with the base flow, the overall

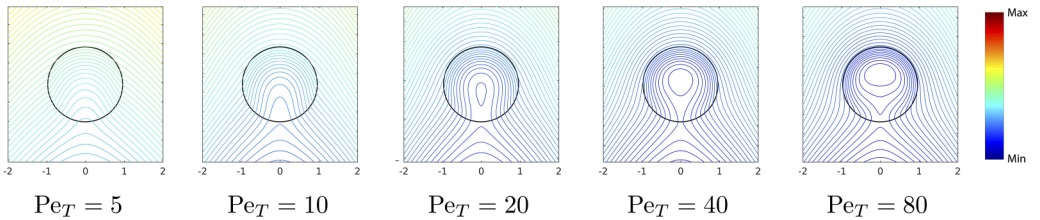FIG. 9. Isotherms for the droplets migrating under a fully developed Poiseuille flow with nonisothermal condition of various Pe_T at time $t = 20$. The numerical results at the 2D slice $(x, y = 0, z)$ are shown here. The colored lines stand for the isotherms, and the black solid line stands for the droplet interface. The contour $c = 0.5$ is used as an approximation for the droplet interface.
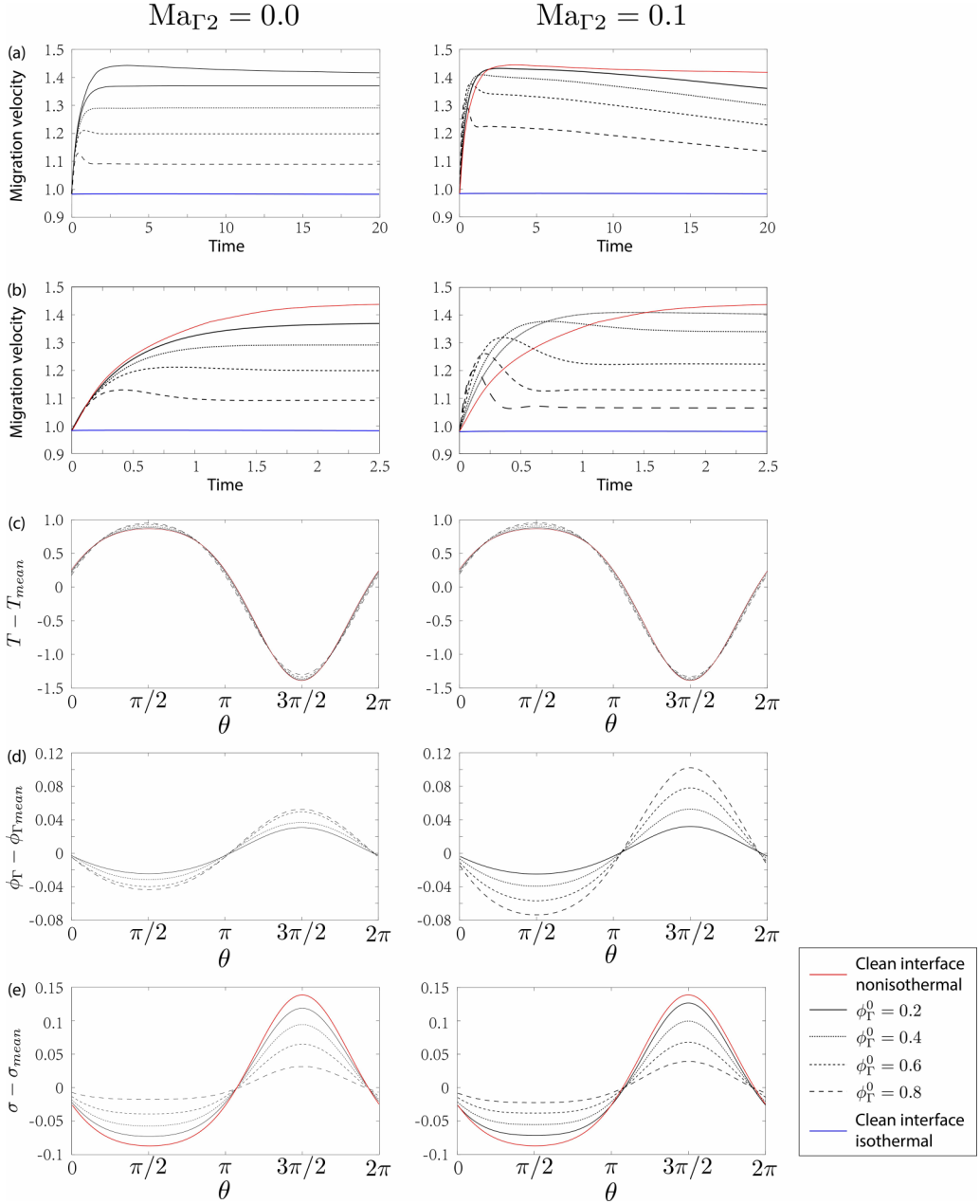
FIG. 10. Droplets covered by insoluble surfactants migrate under a fully developed Poiseuille flow with a nonisothermal condition. The results for two cases, one without the nonlinear coupling term ($Ma_{\Gamma 2} = 0$ left) and the other with it ($Ma_{\Gamma 2} = 0.1$ right), with various initial interface surfactant concentrations ϕ_Γ^0 up to (at) time $t = 20$ are presented. (a) Evolution of migration velocities of droplets covered by surfactant (black lines), a droplet with clean interface under a nonisothermal condition (red solid line), and a droplet with clean interface under an isothermal condition (blue line), respectively. (b) Zoom in of (a). (c)–(e) The interface surfactant concentration, temperature, and surface tension along the droplet interface, respectively. These quantities are plotted as the functions of an angle θ in the 2D plane ($x, y = 0, z$) at time $t = 20$. Here the angle θ is obtained anticlockwise while treating the droplet center as the origin, where $\theta = \pi/2$ stands for the droplet front, and $\theta = 3\pi/2$ stands for the droplet rear. For simplicity, all quantities in (c)–(e) are subtracted by their mean values over the interface.

temperature around the droplet keeps increasing. The surfactant-induced Marangoni force becomes stronger comparing to the thermal-induced Marangoni force, which decreases the migration velocity gradually. Therefore, we term it the quasi-steady-state velocity for the case with nonlinear coupling term $\mathrm{Ma}_{\Gamma 2} > 0$.

2. Effects of the Péclet number Pe_Γ

We next examine the effects of the interface surfactant Péclet number Pe_Γ. Figure 11 shows the numerical results for various Pe_Γ at time $t = 20$ with low surfactant concentration ($\phi_\Gamma^0 = 0.2$) and high surfactant concentration ($\phi_\Gamma^0 = 0.8$), respectively. It can be observed that the terminal migration velocity decreases as we increase Pe_Γ; this is because a weaker diffusion (larger Pe_Γ) increases the variation of the surfactant along the droplet interface. As indicated in the previous section, the surfactant-induced Marangoni force always opposes the thermal-induced Marangoni force, therefore the higher surfactant gradient along the droplet interface would in turn keep the surface tension more uniform along the droplet interface, and eventually weakens the thermal-induced Marangoni force and thus reduces the migration velocity. Moreover, comparing the two cases in Fig. 11(b), we observe that for an initially higher surfactant concentration ($\phi_\Gamma^0 = 0.8$), the variations of the droplet migration velocities are much larger in the initial stage, and the velocities reach their quasi-steady states much faster than that of low surfactant concentration ($\phi_\Gamma^0 = 0.2$). In addition, the surfactant-induced retardations are more obvious for the high surfactant concentration case, where the terminal migration velocity with $\mathrm{Pe}_\Gamma = 8$ becomes even lower than that of a clean interface under isothermal condition. This further reveals that the thermal-induced and surfactant-induced Marangoni forces are more competitive under high surfactant concentration.

3. Effect of the surfactant Marangoni number $Ma_{\Gamma 2}$

Finally, we examine the effect of the nonlinear coupling term $\mathrm{Ma}_{\Gamma 2}\, T \ln(1 - \phi_\Gamma)$ that appears in the surface tension. In Fig. 12 we show the numerical results for various $\mathrm{Ma}_{\Gamma 2}$ with low ($\phi_\Gamma^0 = 0.2$) and high ($\phi_\Gamma^0 = 0.8$) surfactant concentrations, respectively, at time $t = 20$. It can be observed that for both low- and high-concentration cases, when the coupling term appears in the surface tension ($\mathrm{Ma}_{\Gamma 2} > 0$), the initial migration velocities are always larger than that of the droplet with a clean interface, and meanwhile the initial acceleration effect is much stronger in high concentration case. This indicates that this term strengthens the thermal-induced Marangoni force at the early stage, which becomes larger with a higher surfactant concentration. Moreover, the accelerating period is much shorter for a higher surfactant concentration. After the acceleration stage, the velocities decrease for both cases and eventually become lower than that of the droplet with a clean interface. In addition, for the high-concentration case, the velocity variations are much stronger in the initial period, where the velocities reach their quasi-steady state much faster than those cases with low concentration. This indicates that the nonlinear coupling term would also strengthen the surfactant-induced Marangoni force that opposes the thermal-induced Marangoni force, which becomes larger as we increase ϕ_Γ^0. On the other hand, when this term disappears, the migration velocities are always lower than that of clean interface and reach their steady state after a short period. For both cases, the terminal migration velocities increase as $\mathrm{Ma}_{\Gamma 2}$ increases.

Again, the terminal migration velocities slightly decrease for any $\mathrm{Ma}_{\Gamma 2} > 0$ as time passes, whereas for $\mathrm{Ma}_{\Gamma 2} = 0$, the terminal velocities stay steady. See the discussion in Sec. IV B 1. Finally, we show the terminal velocities at time $t = 20$ vs Pe_Γ and $\mathrm{Ma}_{\Gamma 2}$ in Figs. 13(a) and 13(b), respectively. It can be observed that as we increase $\mathrm{Ma}_{\Gamma 2}$, the terminal velocities also increase for all the values of ϕ_Γ^0, which, again, indicates that the surface tension becomes more sensitive to the temperature as we increase ϕ_Γ^0. Moreover, the terminal velocities for the high concentration case are always lower than those for the low concentration case, indicating that the surfactant-induced Marangoni force becomes stronger as we increase ϕ_Γ^0, which would in turn lower the effects of the thermal-induced Marangoni force, and thus reduces the terminal velocities.

FIG. 11. Droplets covered by insoluble surfactants migrate under a fully developed Poiseuille flow with a nonisothermal condition. The results for two cases, one with low surfactant concentration ($\phi_\Gamma^0 = 0.2$ left) and one with high concentration ($\phi_\Gamma^0 = 0.8$ right), with various Pe_Γ up to (at) time $t = 20$ are presented. (a) Evolution of migration velocities of droplets covered by surfactant (black lines), a droplet with a clean interface under a nonisothermal condition (red solid line) and a droplet with a clean interface under an isothermal condition (blue line). (b) Zoom in of (a). (c)–(e) Interface surfactant concentration, temperature. and surface tension along the droplet interface, respectively. These quantities are plotted as the functions of an angle θ in the 2D plane ($x, y = 0, z$) at time $t = 20$. The angle θ is obtained anticlockwise while treating the droplet center as the origin, where $\theta = \pi/2$ stands for the droplet front, and $\theta = 3\pi/2$ stands for the droplet rear. For simplicity, all quantities in (c–e) are subtracted by their mean values over the interface.
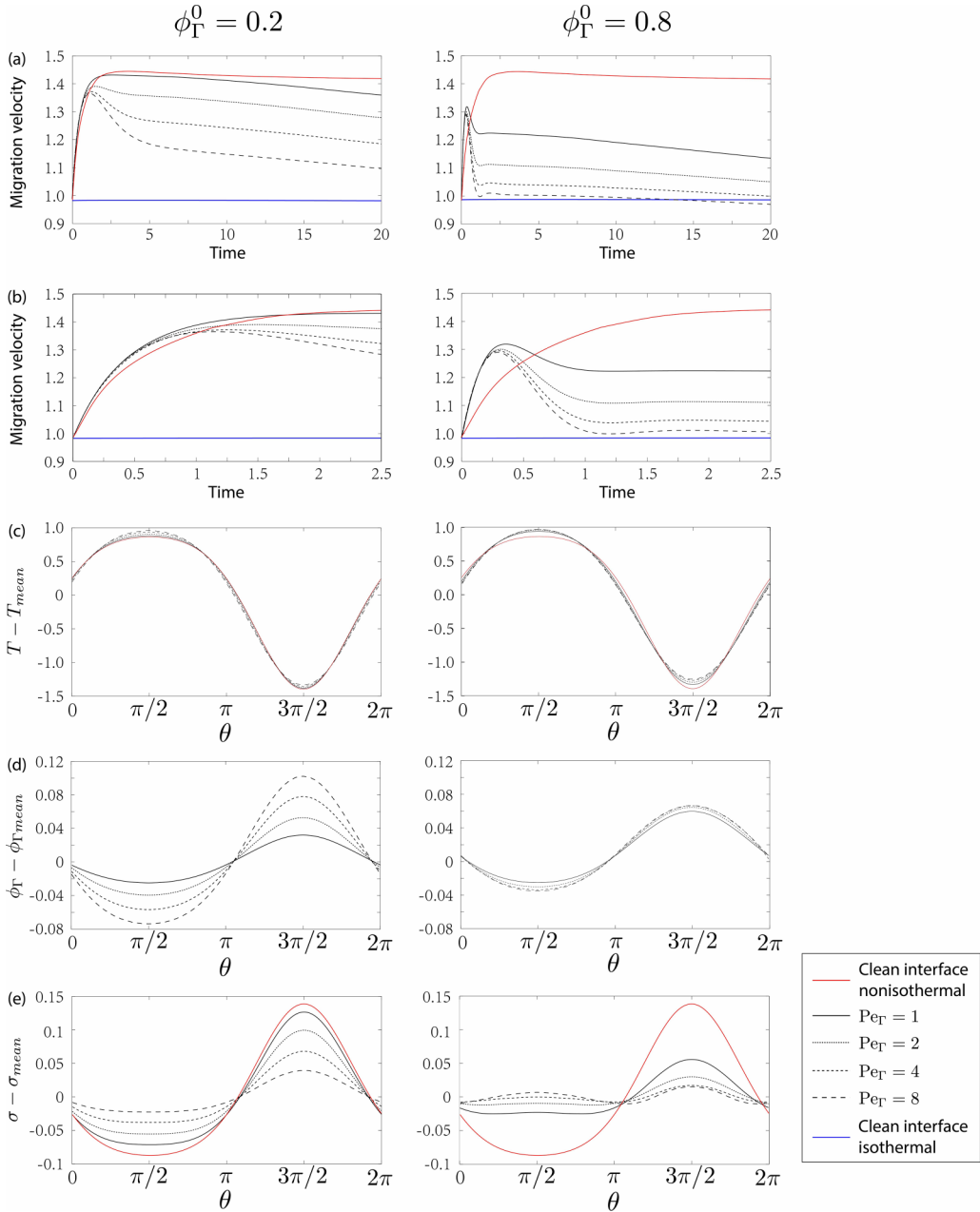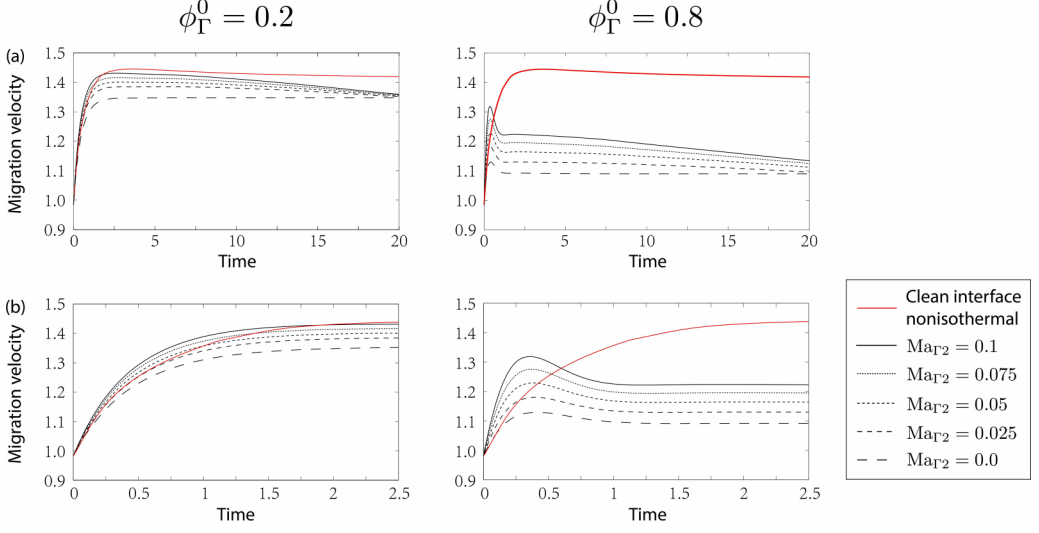
FIG. 12. Droplets covered by insoluble surfactants migrate under a fully developed Poiseuille flow with a nonisothermal condition. The results for two cases, one with low surfactant concentration ($\phi_\Gamma^0 = 0.2$ left) and one with high concentration ($\phi_\Gamma^0 = 0.8$ right), with various $\mathrm{Ma}_{\Gamma2}$ at time $t = 20$ are presented. (a) Evolution of migration velocities of a droplets with a clean interface under nonisothermal condition (red solid line) and droplets covered by surfactant (black lines), respectively. (b) Zoom in of (a).

V. CONCLUSION

In this study we present a three-dimensional numerical study for the nonlinear coupling effects of the thermocapillarity and insoluble surfactants on droplet migration in a square microchannel under a fully developed Poiseuille flow. A thermodynamically consistent diffuse-domain model is developed for simulating the two-phase flows with the coupling of thermocapillary effects and soluble and insoluble surfactants. As the temperature and surfactants are introduced to the internal energy, entropy, and free energy for the two-phase flows, the model recovers the classical Langmuir equation of state for the surface tension, introducing a nonlinear coupling term of surfactant concentration and temperature, which allows us to investigate the case with high surfactant concentration.

The model is based on a diffuse interface framework, which can capture the evolution of the fluid-fluid interface and surfactant concentration easily and accurately. Three numerical tests are carried out to validate our model and the numerical methods. In the first numerical test, we simulate
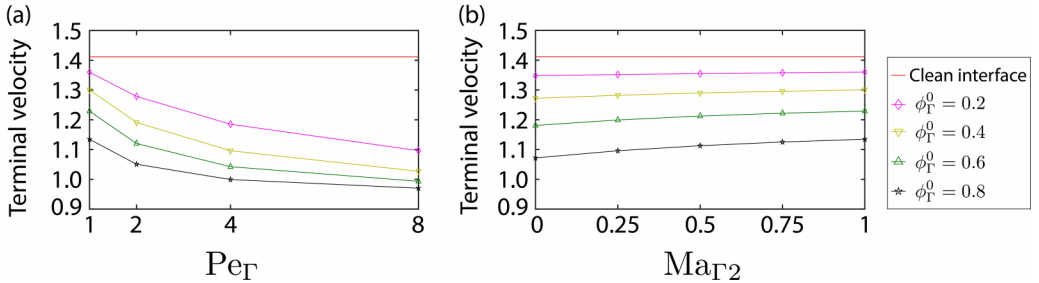

FIG. 13. Terminal velocities at time $t = 20$ for various initial surfactant concentration ϕ_Γ^0 vs (a) the interface surfactant Péclet number Pe_Γ and (b) the surfactant Marangoni number $\mathrm{Ma}_{\Gamma2}$ of the nonlinear coupling term.

the thermocapillary migration in the microchannel where the droplet migration is induced only by the temperature gradient. The numerical results show that our phase-field model for two phase flows converges to the sharp-interface model asymptotically. In the second test, we simulate the motion of a droplet with clean interface in a square microchannel under a fully developed Poiseuille flow, where the isothermal condition is considered. The result shows that the evolution of the droplet deformation agrees well with those from several existing numerical methods, including BEM, LBM, and FTM. In the last test, we consider the interface surfactant diffusion on a stationary and a moving circle, respectively, which validates the diffuse-domain representation for the interface surfactant equation. Comparing to the analytical solution on the sharp interface, we show that our diffuse-domain representation converges to the sharp-interface model, achieving a second-order accuracy with respect to the diffuse interface thickness ϵ.

Finally, we numerically investigate the nonlinear coupling effects of thermocapillarity and insoluble surfactants on droplet migration in a square microchannel under a fully developed Poiseuille flow. We find that the surfactant-induced Marangoni force always opposes the thermal-induced Marangoni force, where the surfactant-covered droplet always migrates slower than that without surfactant. The retardation to the migration velocity is stronger as we increase the initial surfactant concentration ϕ_Γ^0. In addition, the surfactant has a stabilization effect subsequently, where as long as the droplet is covered by surfactant, the migration velocity would reach its (quasi) steady state faster than that of the droplet with a clean interface. The stabilization effect also becomes stronger as we increase ϕ_Γ^0.

Moreover, we find that the appearance of the nonlinear coupling term $\mathrm{Ma}_{\Gamma 2} T \log(1 - \phi_\Gamma)$ in the surface tension introduces extra effects to the droplet migration. First, it introduces an extra acceleration effect to the droplet migration at early stage. As long as the nonlinear coupling term appears ($\mathrm{Ma}_{\Gamma 2} > 0$), the initial velocity of a surfactant-covered droplet is larger than that without a surfactant. However, when the nonlinear coupling term disappears ($\mathrm{Ma}_{\Gamma 2} = 0$), the initial velocity of a surfactant-covered droplet is always smaller than that with clean interface. Second, with the appearance of this term ($\mathrm{Ma}_{\Gamma 2} > 0$), the terminal migration velocity of the surfactant-covered droplet decreases gradually as time passes, leading to a a quasi-steady state, whereas without this term ($\mathrm{Ma}_{\Gamma 2} = 0$) the terminal velocity of a surfactant-covered droplet stays steady. This is due to the fact that as the droplet migrates upward with the base flow, the overall temperature around the droplet increases. The extra surfactant-induced Marangoni force is introduced by this nonlinear coupling term, which becomes stronger as temperature increases and thus weakens the thermal-induced Marangoni force and decreases the migration velocity gradually.

In future work, we intend to explore the effect of solubility of the surfactant by considering the soluble surfactants. We also plan to investigate the convergence for our diffuse-domain model through the asymptotic analysis and more numerical simulations.

APPENDIX A: MODEL DERIVATIONS

Here we show the derivations of our model equations, where we use a phase-field model for simulating the two-phase flows, and a diffuse domain model for the insoluble surfactants on the fluid-fluid interface. The model derivations are done by following a thermodynamically consistent framework that ensures the conservation laws of the system.

1. Mass conservation for the surfactants of sharp-interface model

We start by considering the sharp-interface model for insoluble surfactants. Consider a domain $\Omega \subset \mathbb{R}^3$ with a fluid-fluid interface $\Gamma(t)$, where the interior of the interface, $\Omega_1(t) \subset \Omega$, is of fluid

1, the exterior, $\Omega_2(t) \subset \Omega$, is of fluid 2, and $\partial\Omega$ is the solid boundary. As derived by [74], the mass conservation of interface surfactants for a sharp-interface model yields

$$\partial_t \phi_\Gamma + \boldsymbol{v} \cdot \boldsymbol{\nabla}\phi_\Gamma + \phi_\Gamma \boldsymbol{\nabla}_\Gamma \cdot \boldsymbol{v} = -\boldsymbol{\nabla}_\Gamma \cdot \boldsymbol{q}_{\phi_\Gamma} \qquad \text{on } \Gamma(t), \tag{A1}$$

where ϕ_Γ is the interface surfactant concentrations on $\Gamma(t)$, $\boldsymbol{v}$ is the velocity field, $\boldsymbol{\nabla}_\Gamma = \boldsymbol{\nabla} - \boldsymbol{n}_\Gamma(\boldsymbol{n}_\Gamma \cdot \boldsymbol{\nabla})$ is the surface gradient operator, and $\boldsymbol{n}_\Gamma$ is the external unit normal of Γ pointing from fluid 1 to fluid 2, and $\boldsymbol{q}_{\phi_\Gamma}$ is the corresponding molecular flux.

2. Phase-field method for two-phase flows

For simulating the two-phase incompressible fluid flows, we apply the phase-field method by treating the two fluids as one mixture with variable properties. The fluid-fluid interface $\Gamma(t)$ is then extended into an interfacial region with finite thickness, and a phase variable c is defined over the entire domain Ω to characterize the two fluids, which takes a different constant for each fluid component and changes continuously and rapidly across the interfacial region. Here we employ the volume fraction c of fluid 1 as the phase variable and define the following variable density for the mixture:

$$\rho(c) = \rho_1 c + \rho_2(1 - c), \tag{A2}$$

where ρ_i is constant density for the ith incompressible fluid component. The variable density ρ then yields the mass conservation:

$$\partial_t \rho + \boldsymbol{\nabla} \cdot (\boldsymbol{v}\rho) = 0, \tag{A3}$$

where $\boldsymbol{v}$ stands for the mass averaged velocity. Here we refer to [46] for the detailed definition of $\boldsymbol{v}$ and the corresponding derivations. Moreover, we define the following function to characterize the fluid-fluid interface $\Gamma(t)$:

$$\delta(c, \boldsymbol{\nabla}c) = \eta\left(h(c) + \epsilon\frac{|\boldsymbol{\nabla}c|^2}{2}\right) = \eta\left(\frac{c^2(1-c)^2}{4\epsilon} + \epsilon\frac{|\boldsymbol{\nabla}c|^2}{2}\right), \tag{A4}$$

where $\delta(c \cdot \boldsymbol{\nabla}c)$ is the Cahn-Hilliard-type free energy density for $\Gamma(t)$, $h(c)$ the double-well free energy, and ϵ a small parameter characterizing the thickness of the interfacial region. In addition, $\eta = 6\sqrt{2}$ is the ratio parameter that relates the surface tension of the sharp-interface model to that of the phase-field model [46,64]. For simplicity, we use the shorter notations ρ and δ in the present paper.

Following the diffuse-domain formulations in [61], the original sharp-interface interface surfactant Eq. (A1) is then extended from $\Gamma(t)$ to Ω by coupling with δ, such that

$$\frac{D(\delta\phi_\Gamma)}{Dt} = -\delta\phi_\Gamma\boldsymbol{\nabla} \cdot \boldsymbol{v} - \boldsymbol{\nabla} \cdot (\delta\boldsymbol{q}_{\phi_\Gamma}). \tag{A5}$$

3. Internal energy, entropy, and free energy

As the thermocapillary effects and insoluble surfactants are considered simultaneously, we expect that the free energy of the fluid-fluid interface depends on both the temperature field T and interface surfactant concentration ϕ_Γ. Following the framework by [46], the internal energy, entropy, and free energy densities for the two-phase incompressible fluid can be given by

$$\hat{u}(s, \rho, c, \boldsymbol{\nabla}c, \phi_\Gamma) = u(s, \rho) + \delta\gamma_u(\phi_\Gamma), \tag{A6}$$

$$\hat{s}(T, \rho, c, \boldsymbol{\nabla}c, \phi_\Gamma) = s(T, \rho) + \delta\gamma_s(\phi_\Gamma), \tag{A7}$$

$$\hat{f}(T, \rho, c, \boldsymbol{\nabla}c, \phi_\Gamma) = f(T, \rho) + \delta\gamma_f(\phi_\Gamma, T). \tag{A8}$$

Here u, s, and f are the classical parts [46] that can be defined as

$$u = \rho c_{hc}(T - T_0), \tag{A9}$$

$$s = \rho c_{hc} \ln\left(\frac{T}{T_0}\right), \tag{A10}$$

$$f = \rho c_{hc}(T - T_0) - \rho c_{hc} T \ln\left(\frac{T}{T_0}\right), \tag{A11}$$

where u_0 is the reference internal energy corresponding to reference temperature T_0, and c_{hc} is the heat capacity. Here we assume that $T > T_0$, γ_u, γ_s, and γ_f are the corresponding energy, entropy, and free energy for the fluid-fluid interface. Moreover, we denote the following thermodynamic relations:

$$\hat{f} = \hat{u} - T\hat{s},$$
$$f = u - Ts,$$
$$\gamma_f(\phi_\Gamma, T) = \gamma_u(\phi_\Gamma) - T\gamma_s(\phi_\Gamma). \tag{A12}$$

In particular, we specify these terms to recover the classical Langmuir equation of state:

$$\gamma_u(\phi_\Gamma) = \tilde{\sigma}_0|_{T=T_0} + \mu_\gamma \phi_\Gamma - T_0 \frac{\partial \tilde{\sigma}_0}{\partial T} = \sigma_0 + \mu_\gamma \phi_\Gamma - T_0 \frac{\partial \tilde{\sigma}_0}{\partial T}, \tag{A13}$$

$$\gamma_s(\phi_\Gamma) = -\frac{\partial \tilde{\sigma}_0}{\partial T} - R\left[\phi_\Gamma \ln\frac{\phi_\Gamma}{\phi_\Gamma^\infty} + (\phi_\Gamma^\infty - \phi_\Gamma)\ln\left(1 - \frac{\phi_\Gamma}{\phi_\Gamma^\infty}\right)\right], \tag{A14}$$

$$\gamma_f(\phi_\Gamma, T) = \gamma_u(\phi_\Gamma) - T\gamma_s(\phi_\Gamma)$$
$$= \sigma_0 + \mu_\gamma \phi_\Gamma + \frac{\partial \tilde{\sigma}_0}{\partial T}(T - T_0) + RT\left[\phi_\Gamma \ln\frac{\phi_\Gamma}{\phi_\Gamma^\infty} + (\phi_\Gamma^\infty - \phi_\Gamma)\ln\left(1 - \frac{\phi_\Gamma}{\phi_\Gamma^\infty}\right)\right], \tag{A15}$$

where $\tilde{\sigma}_0$ is the surface tension of the surfactant-free interface, $\sigma_0 = \tilde{\sigma}_0|_{T=T_0}$ is the reference surface tension corresponding to T_0, $\partial \tilde{\sigma}_0/\partial T$ (< 0) is a constant representing for the derivative of the surfactant-free surface tension σ_0 with respect to temperature, μ_γ is the standard chemical potentials, ϕ_Γ^∞ the surfactant concentrations at saturation on the fluid-fluid interface, and R is the gas constant. Note that the above definitions are obtained by following the derivation framework that was introduced in [75], where the surface tension and surface chemical potential were obtained by using the surface free energy (A15). The surface tension $\sigma_f(\phi_\Gamma, T)$ is then obtained through the Legendre transform of $\gamma_f(\phi_\Gamma, T)$, such that

$$\sigma_f(\phi_\Gamma, T) = \gamma_f(\phi_\Gamma, T) - \frac{\partial \gamma_f(\phi_\Gamma, T)}{\partial \phi_\Gamma}\phi_\Gamma = \sigma_0 + \frac{\partial \tilde{\sigma}_0}{\partial T}(T - T_0) + RT\phi_\Gamma^\infty \ln\left(1 - \frac{\phi_\Gamma}{\phi_\Gamma^\infty}\right). \tag{A16}$$

Here the surface tension depends on both the temperature field and interface surfactant concentration in a nonlinear coupling way, which not only consists of a classical linear part for thermocapillary effects, but also recovers the Langmuir equation of state for the surface tension under nonisothermal condition. Moreover, our derivation for (A16) recovers the result obtained by [76], which also considers the nonlinear coupling effects of thermocapillarity and surfactants to the droplet migration. In their work the temperature-dependent part of the surface tension, $\frac{\partial \tilde{\sigma}_0}{\partial T}(T - T_0)$, is derived by expanding the surfactant-free surface tension σ_0 at the reference temperature T_0.

4. Conservation laws

We next define the physical quantities and the corresponding conservation laws for the two-phase fluid flows. Suppose the two-fluid fills in a domain Ω, we then take an arbitrary material volume

$V(t) \in \Omega$ that moves with the mixture, and define the total mass M, volume of single fluid C, momentum $\boldsymbol{P}$, energy E, and entropy S as follows:

$$M = \int_{V(t)} \rho \, dV, \tag{A17}$$

$$C = \int_{V(t)} c \, dV, \tag{A18}$$

$$\boldsymbol{P} = \int_{V(t)} \rho \boldsymbol{v} \, dV, \tag{A19}$$

$$E = \int_{V(t)} \frac{1}{2} \rho |\boldsymbol{v}|^2 + \hat{u} \, dV, \tag{A20}$$

$$S = \int_{V(t)} \hat{s} \, dV, \tag{A21}$$

where ρ is defined in Eq. (A2), $\boldsymbol{v}$ the mass averaged velocity of the mixture [56,64], and $\hat{u}$ and $\hat{s}$ are energy and entropy densities defined in Eqs. (A6) and (A7). The corresponding conservation laws can be given by

$$\frac{dM}{dt} = 0, \tag{A22}$$

$$\frac{dC}{dt} = \int_{\partial V(t)} -\boldsymbol{q}_C \cdot \boldsymbol{n} \, dA, \tag{A23}$$

$$\frac{d\boldsymbol{P}}{dt} = \int_{\partial V(t)} \mathbf{m} \cdot \boldsymbol{n} \, dA, \tag{A24}$$

$$\frac{dE}{dt} = \int_{\partial V(t)} \boldsymbol{v} \cdot \mathbf{m} \cdot \boldsymbol{n} - \boldsymbol{q}_E \cdot \boldsymbol{n} - \boldsymbol{q}_E^{nc} \cdot \boldsymbol{n} \, dA, \tag{A25}$$

$$\frac{dS}{dt} = \int_{\partial V(t)} -\frac{\boldsymbol{q}_E}{T} \cdot \boldsymbol{n} - \boldsymbol{q}_S^{nc} \cdot \boldsymbol{n} \, dA + \int_{V(t)} S_{\text{gen}} \, dV \quad (S_{\text{gen}} \geqslant 0). \tag{A26}$$

Here Eq. (A22) represents the mass conservation of the mixture within $V(t)$, and Eq. (A23) stands for the volume conservation of a single fluid (here for fluid 1), where $\boldsymbol{q}_C$ is the volume flux of fluid 1 through the boundary $\partial V(t)$ with the external unit normal $\boldsymbol{n}$ of the volume $V(t)$. The momentum conservation (A24) states that the rate of change in total momentum equals the surface forces $\mathbf{m}$ acting on the volume boundary (here we ignore the body force). The energy conservation (A25) states that the change in total energy equals the rate of work done by the forces $\mathbf{m}$ on the boundary plus the energy flux (including the classical $\boldsymbol{q}_E$ and nonclassical $\boldsymbol{q}_E^{nc}$ internal energy flux) through the boundary $\partial V(t)$. The entropy conservation Eq. (A26) states that the rate of change of entropy in $V(t)$ during the process equals the net entropy transfer through the boundary (including the classical $\boldsymbol{q}_E/T$ and nonclassical $\boldsymbol{q}_S^{nc}$ entropy flux) plus the local entropy generation S_{gen}. Based on the second law of thermodynamics, the local entropy generation is nonnegative ($S_{\text{gen}} \geqslant 0$) for a dissipative system (or, say, for an irreversible process), which is the key to the thermodynamically consistent framework [46] that we used for the derivations.

5. Entropy generation

Substituting the definitions (A17)–(A21) into the conservation laws (A22)–(A26), and using the thermodynamic relations, we obtain the entropy generation of the system

$$\int_{V(t)} S_{\text{gen}} \, dV = \int_{V(t)} \nabla \cdot \left[-\frac{1}{T} \left(\boldsymbol{q}_E^{nc} - f_E^{nc} \right) + \boldsymbol{q}_S^{nc} + \eta \epsilon \sigma_s(\phi_\Gamma) \frac{Dc}{Dt} \nabla c \right] + \left(\boldsymbol{q}_E^{nc} - f_E^{nc} \right) \cdot \nabla \frac{1}{T}$$

$$+ \frac{1}{T} \boldsymbol{\tau} : \nabla \boldsymbol{v} - \frac{1}{T} \nabla \mu_c \cdot \boldsymbol{q}_C + \nabla \frac{1}{T} \cdot \boldsymbol{q}_E - \frac{\delta}{T} \frac{\partial^2 \gamma_f}{\partial \phi_\Gamma^2} \nabla \phi_\Gamma \cdot \boldsymbol{q}_{\phi_\Gamma} \, dV. \tag{A27}$$

Here we refer to Appendixes B and C for the detailed derivations. To ensure $S_{\text{gen}} \geqslant 0$, we specify the unknown terms, including $\boldsymbol{q}_C$, $\boldsymbol{q}_E$, $\boldsymbol{q}_E^{nc}$, $\boldsymbol{q}_S^{nc}$, $\mathbf{m}$, $\boldsymbol{\tau}$, and $\boldsymbol{q}_{\phi_\Gamma}$ (see Appendix C 2), such that we show the nonnegativity of the entropy generation of our system equations:

$$\int_{V(t)} S_{\text{gen}} \, dV = \int_{V(t)} k \frac{|\boldsymbol{\nabla} T|^2}{|T|^2} + \frac{1}{T} m_c |\boldsymbol{\nabla} \mu_c|^2 + \frac{1}{T} \boldsymbol{\tau} : \boldsymbol{\nabla} \boldsymbol{v} + \frac{1}{T} \delta \frac{\partial^2 \gamma_f}{\partial \phi_\Gamma^2} m_{\phi_\Gamma} |\boldsymbol{\nabla} \phi_\Gamma|^2 \, dV \geqslant 0. \quad \text{(A28)}$$

6. Model equations

We next substitute all these terms into the conservation laws (A22)–(A25) to obtain the model equations. Together with the interface surfactant (A5), the diffuse interface model for the two-phase flows with thermocapillary effects and insoluble surfactants is given by

$$\rho \boldsymbol{v}_t + \rho \boldsymbol{v} \cdot \boldsymbol{\nabla} \boldsymbol{v} = \boldsymbol{\nabla} \cdot \mathbf{m}, \quad \text{(A29)}$$

$$\boldsymbol{\nabla} \cdot \boldsymbol{v} = \boldsymbol{\nabla} \cdot (\alpha m_c \boldsymbol{\nabla} \mu_c), \quad \text{(A30)}$$

$$c_t + \boldsymbol{\nabla} \cdot (\boldsymbol{v} c) = \boldsymbol{\nabla} \cdot (m_c \boldsymbol{\nabla} \mu_c), \quad \text{(A31)}$$

$$(\delta \phi_\Gamma)_t + \boldsymbol{\nabla} \cdot (\boldsymbol{v} \delta \phi_\Gamma) = \boldsymbol{\nabla} \cdot (m_{\phi_\Gamma} \delta \boldsymbol{\nabla} \phi_\Gamma), \quad \text{(A32)}$$

$$[\rho c_{hc}(T - T_0)]_t + \boldsymbol{\nabla} \cdot [\boldsymbol{v} \rho c_{hc}(T - T_0)] = \boldsymbol{\nabla} \cdot [k \boldsymbol{\nabla}(T - T_0)] + h_s, \quad \text{(A33)}$$

where

$$\mathbf{m} = \sigma_f(\phi_\Gamma, T)[\delta \mathbf{I} - \eta \epsilon (\boldsymbol{\nabla} c \otimes \boldsymbol{\nabla} c)] - \tilde{p} \mathbf{I} + \boldsymbol{\tau} - p \mathbf{I}, \quad \text{(A34)}$$

$$\sigma_f(\phi_\Gamma, T) = \sigma_0 + \partial \tilde{\sigma}/\partial T (T - T_0) + RT \phi_\Gamma^\infty \ln(1 - \phi_\Gamma/\phi_\Gamma^\infty), \quad \text{(A35)}$$

$$\boldsymbol{\tau} = \mu(\boldsymbol{\nabla} \boldsymbol{v} + \boldsymbol{\nabla} \boldsymbol{v}^T) - 2\mu(\boldsymbol{\nabla} \cdot \boldsymbol{v})\mathbf{I}/3, \quad \text{(A36)}$$

$$\mu_c = \eta \sigma_0 \mu_0 + \alpha p, \quad \text{(A37)}$$

$$\mu_0 = h'(c) - \epsilon \Delta c, \quad \text{(A38)}$$

$$m_c = \sqrt{c^2(1-c)^2} + \epsilon. \quad \text{(A39)}$$

Here $\boldsymbol{v}$ is the velocity for the mixture, $\mathbf{m}$ the general stress tensor, $\sigma_f(\phi_\Gamma, T)$ the surface tension, ϕ_Γ the interface surfactant concentration, $\delta(c \cdot \boldsymbol{\nabla} c)$ the Cahn-Hilliard type free energy density for the fluid-fluid interface, and ϵ a small parameter characterizing the thickness of the interfacial region, $\eta = 6\sqrt{2}$ the ratio parameter that relates the surface tension of the sharp-interface model to that of the phase-field model, p the pressure, $\alpha = (\rho_2 - \rho_1)/\rho_2$, m_c and μ_c are the degenerate mobility and chemical potential for the phase field, respectively, and the scalars $\tilde{p}$ and h_s are given by Eqs. (C9) and (C27), respectively. Moreover, the variable properties for the two-phase flows are defined as

$$\Lambda = \Lambda_1 c + \Lambda_2 (1 - c), \quad \text{(A40)}$$

where Λ stands for the variable density ρ, viscosity μ, heat capacity c_{hc}, and heat conductivity k, respectively, and Λ_i is the corresponding constant properties, ρ_i, μ_i, c_{hci}, k_i, of the ith fluid. In addition, the following BCs can be imposed:

$$\boldsymbol{v} = \boldsymbol{v}_b, \quad T = T_b, \quad \boldsymbol{n} \cdot \boldsymbol{\nabla} c = \boldsymbol{n} \cdot \boldsymbol{\nabla} \mu_c = \boldsymbol{n} \cdot \boldsymbol{\nabla} \phi_\Gamma = 0 \quad \text{on} \ \partial \Omega. \quad \text{(A41)}$$

Again, the system equations (A29)–(A33) satisfy the nonnegativity of the entropy generation $S_{\text{gen}} \geqslant 0$ (A28).

APPENDIX B: CONSERVATION LAWS

1. Mass and volume conservation

Substituting Eq. (A17) into Eq. (A22), and using the definition of variable density ρ (A2), we obtain the mass conservation

$$\int_{V(t)} \frac{D\rho}{Dt}\, dV = \int_{V(t)} \frac{d\rho}{dc}\frac{Dc}{Dt}\, dV = \int_{V(t)} (\rho_1 - \rho_2)\frac{Dc}{Dt}\, dV = \int_{V(t)} -\rho\boldsymbol{\nabla}\cdot\boldsymbol{v}\, dV. \qquad (B1)$$

Substituting Eq. (A18) into Eq. (A23), we obtain the volume conservation

$$\int_{V(t)} \frac{Dc}{Dt}\, dV = \int_{V(t)} -c\boldsymbol{\nabla}\cdot\boldsymbol{v} - \boldsymbol{\nabla}\cdot\boldsymbol{q}_C\, dV. \qquad (B2)$$

Substituting Eq. (B1) into Eq. (B2), we obtain

$$\int_{V(t)} \boldsymbol{\nabla}\cdot\boldsymbol{v}\, dV = \int_{V(t)} -\alpha\boldsymbol{\nabla}\cdot\boldsymbol{q}_C\, dV db9 \qquad (B3)$$

or equivalently

$$\int_{V(t)} \frac{Dc}{Dt}\, dV = \int_{V(t)} \left(-c + \frac{1}{\alpha}\right)\boldsymbol{\nabla}\cdot\boldsymbol{v}\, dV, \qquad (B4)$$

where $\alpha = (\rho_2 - \rho_1)/\rho_2$. Note that the velocity $\boldsymbol{v}$ for the binary incompressible fluid is not incompressible due to the variable density along the interfacial region, which is termed as the quasi-incompressibility [56]. This formulation is obtained by following the mass conservation of both the mixture and the single fluid simultaneously.

2. Momentum and energy conservation

Substituting Eq. (A19) into Eq. (A24), we obtain the momentum conservation

$$\int_{V(t)} \rho\frac{D\boldsymbol{v}}{Dt}\, dV = \int_{V(t)} \boldsymbol{\nabla}\cdot\mathbf{m}\, dV. \qquad (B5)$$

Substituting Eq. (A20) into Eq. (A25), we obtain the energy conservation

$$\int_{V(t)} \rho\frac{D\boldsymbol{v}}{Dt}\cdot\boldsymbol{v} + \frac{D\hat{u}}{Dt} + \hat{u}\boldsymbol{\nabla}\cdot\boldsymbol{v}\, dV = \int_{V(t)} \boldsymbol{\nabla}\cdot(\mathbf{m}\cdot\boldsymbol{v}) - \boldsymbol{\nabla}\cdot\boldsymbol{q}_E - \boldsymbol{\nabla}\cdot\boldsymbol{q}_E^{nc}\, dV. \qquad (B6)$$

Multiplying Eq. (B5) by $\boldsymbol{v}$, and substituting into Eq. (B6), we obtain

$$\int_{V(t)} \frac{D\hat{u}}{Dt} + \hat{u}\boldsymbol{\nabla}\cdot\boldsymbol{v}\, dV = \int_{V(t)} \boldsymbol{\nabla}\cdot(\mathbf{m}\cdot\boldsymbol{v}) - \boldsymbol{\nabla}\cdot\mathbf{m}\cdot\boldsymbol{v} - \boldsymbol{\nabla}\cdot\boldsymbol{q}_E - \boldsymbol{\nabla}\cdot\boldsymbol{q}_E^{nc}\, dV. \qquad (B7)$$

With the help of the identities (A6) and

$$\boldsymbol{\nabla}\cdot(\mathbf{m}\cdot\boldsymbol{v}) = \boldsymbol{\nabla}\cdot\mathbf{m}\cdot\boldsymbol{v} + \mathbf{m}:\boldsymbol{\nabla}\boldsymbol{v}, \quad \boldsymbol{\nabla}\cdot\boldsymbol{v} = \mathbf{I}:\boldsymbol{\nabla}\boldsymbol{v}, \qquad (B8)$$

Eq. (B7) can be simplified as

$$\int_{V(t)} \frac{Du}{Dt} + \frac{D}{Dt}[\delta\gamma_u(\phi_\Gamma)]\, dV = \int_{V(t)} (\mathbf{m} - \hat{u}\mathbf{I}):\boldsymbol{\nabla}\boldsymbol{v} - \boldsymbol{\nabla}\cdot\left(\boldsymbol{q}_E + \boldsymbol{q}_E^{nc}\right)\, dV. \qquad (B9)$$

Further calculation gives

$$\int_{V(t)} \frac{D}{Dt}[\delta\gamma_u(\phi_\Gamma)]\, dV = \int_{V(t)} \gamma_u(\phi_\Gamma)\frac{D\delta}{Dt} + \delta\gamma_u'(\phi_\Gamma)\frac{D\phi_\Gamma}{Dt}\, dV$$

$$= \int_{V(t)} \sigma_u(\phi_\Gamma)\frac{D\delta}{Dt} + \gamma_u'(\phi_\Gamma)\frac{D(\delta\phi_\Gamma)}{Dt}\, dV, \qquad (B10)$$

$$\int_{V(t)} \sigma_u(\phi_\Gamma)\frac{D\delta}{Dt} = \int_{V(t)} \eta(\sigma_u(\phi_\Gamma)\mu_0 - \epsilon\boldsymbol{\nabla}\sigma_u(\phi_\Gamma)\cdot\boldsymbol{\nabla}c)\frac{Dc}{Dt}$$

$$+ \boldsymbol{\nabla}\cdot\left[\eta\epsilon\sigma_u(\phi_\Gamma)\frac{Dc}{Dt}\boldsymbol{\nabla}c\right] - \eta\epsilon\sigma_u(\phi_\Gamma)(\boldsymbol{\nabla}c\otimes\boldsymbol{\nabla}c){:}\boldsymbol{\nabla}\boldsymbol{v}\,dV, \tag{B11}$$

$$\sigma_u(\phi_\Gamma) = \gamma_u(\phi_\Gamma) - \gamma_u'(\phi_\Gamma)\phi_\Gamma, \tag{B12}$$

$$\mu_0 = h'(c) - \epsilon\Delta c. \tag{B13}$$

Substituting Eqs. (B10)–(B13) into Eq. (B9), and introducing a constant surface tension σ_0, we rewrite the energy conservation as

$$\int_{V(t)} \frac{Du}{Dt}\,dV = \int_{V(t)} \left[\mathbf{m} + \eta\epsilon\sigma_u(\phi_\Gamma)(\boldsymbol{\nabla}c\otimes\boldsymbol{\nabla}c) - \hat{u}\mathbf{I}\right]{:}\boldsymbol{\nabla}\boldsymbol{v} - \boldsymbol{\nabla}\cdot\left[\boldsymbol{q}_E + \boldsymbol{q}_E^{nc} + \eta\epsilon\sigma_u(\phi_\Gamma)\frac{Dc}{Dt}\boldsymbol{\nabla}c\right]$$

$$- (\lambda_u + \eta\sigma_0\mu_0)\frac{Dc}{Dt} - \gamma_u'(\phi_\Gamma)\frac{D(\delta\phi_\Gamma)}{Dt}\,dV, \tag{B14}$$

where

$$\lambda_u = \eta[\sigma_u(\phi_\Gamma) - \sigma_0]\mu_0 - \eta\epsilon\boldsymbol{\nabla}\sigma_u(\phi_\Gamma)\cdot\boldsymbol{\nabla}c. \tag{B15}$$

3. Entropy conservation

Substituting Eq. (A21) into Eq. (A26), and using the definition of $\hat{s}$ (A7) and the identity (B8), we obtain the entropy conservation

$$\int_{V(t)} \frac{Ds}{Dt} + \frac{D}{Dt}(\delta\gamma_s(\phi_\Gamma))\,dV = \int_{V(t)} -\boldsymbol{\nabla}\cdot\left(\frac{\boldsymbol{q}_E}{T}\right) - \boldsymbol{\nabla}\cdot\boldsymbol{q}_S^{nc} - \hat{s}\mathbf{I}{:}\boldsymbol{\nabla}\boldsymbol{v} + S_{\text{gen}}\,dV. \tag{B16}$$

We then follow the steps of Eqs. (B10)–(B13) to rewrite the entropy conservation as

$$\int_{V(t)} \frac{Ds}{Dt}\,dV = \int_{V(t)} [\eta\epsilon\sigma_s(\phi_\Gamma)(\boldsymbol{\nabla}c\otimes\boldsymbol{\nabla}c) - \hat{s}\mathbf{I}]{:}\boldsymbol{\nabla}\boldsymbol{v} - \boldsymbol{\nabla}\cdot\left[\frac{\boldsymbol{q}_E}{T} + \boldsymbol{q}_S^{nc} + \eta\epsilon\sigma_s(\phi_\Gamma)\frac{Dc}{Dt}\boldsymbol{\nabla}c\right]$$

$$- \lambda_s\frac{Dc}{Dt} - \gamma_s'(\phi_\Gamma)\frac{D(\delta\phi_\Gamma)}{Dt} + S_{\text{gen}}\,dV, \tag{B17}$$

where we denote

$$\sigma_s(\phi_\Gamma) = \gamma_s(\phi_\Gamma) - \gamma_s'(\phi_\Gamma)\phi_\Gamma, \tag{B18}$$

$$\lambda_s = \eta\sigma_s(\phi_\Gamma)\mu_0 - \eta\epsilon\boldsymbol{\nabla}\sigma_s(\phi_\Gamma)\cdot\boldsymbol{\nabla}c. \tag{B19}$$

APPENDIX C: ENTROPY GENERATION

1. Derivation of the entropy generation

Here we show the derivations for the entropy generation (A27). By applying the thermodynamic relation $\frac{Du}{Dt} = T\frac{Ds}{Dt}$, we rewrite Eq. (B14) to obtain

$$\int_{V(t)} \frac{Ds}{Dt}\,dV = \int_{V(t)} \frac{1}{T}[\mathbf{m} + \eta\epsilon\sigma_u(\phi_\Gamma)(\boldsymbol{\nabla}c\otimes\boldsymbol{\nabla}c) - \hat{u}\mathbf{I}]{:}\boldsymbol{\nabla}\boldsymbol{v} - \frac{1}{T}\boldsymbol{\nabla}\cdot\left(\boldsymbol{q}_E + \boldsymbol{q}_E^{nc}\right)$$

$$- \frac{1}{T}(\lambda_u + \eta\sigma_0\mu_0)\frac{Dc}{Dt} - \frac{1}{T}\boldsymbol{\nabla}\cdot\left[\eta\epsilon\sigma_u(\phi_\Gamma)\frac{Dc}{Dt}\boldsymbol{\nabla}c\right] - \frac{1}{T}\gamma_u'(\phi_\Gamma)\frac{D(\delta\phi_\Gamma)}{Dt}\,dV, \tag{C1}$$

where both sides are divided by T. Substituting Eq. (B17) into the above, we obtain

$$
\begin{aligned}
\int_{V(t)} S_{\text{gen}}\, dV &= \int_{V(t)} \frac{1}{T}\{\mathbf{m} + \eta\epsilon[\sigma_u(\phi_\Gamma) - T\sigma_s(\phi_\Gamma)](\boldsymbol{\nabla} c \otimes \boldsymbol{\nabla} c) - (\hat{u} - T\hat{s})\mathbf{I}\}{:}\boldsymbol{\nabla} \boldsymbol{v} \\
&\quad - \frac{1}{T}\boldsymbol{\nabla}\cdot\left[\boldsymbol{q}_E + \boldsymbol{q}_E^{nc} + \eta\epsilon\sigma_u(\phi_\Gamma)\frac{Dc}{Dt}\boldsymbol{\nabla} c\right] + \boldsymbol{\nabla}\cdot\left[\frac{\boldsymbol{q}_E}{T} + \boldsymbol{q}_S^{nc} + \eta\epsilon\sigma_s(\phi_\Gamma)\frac{Dc}{Dt}\boldsymbol{\nabla} c\right] \\
&\quad - \frac{1}{T}(\lambda_u - T\lambda_s + \eta\sigma_0\mu_0)\frac{Dc}{Dt} - \frac{1}{T}[\gamma_u'(\phi_\Gamma) - T\gamma_s'(\phi_\Gamma)]\frac{D(\delta\phi_\Gamma)}{Dt}\, dV.
\end{aligned}
\tag{C2}
$$

We now define the surface tension as the Legendre transform of $\gamma_f(\phi_\Gamma, T)$

$$
\begin{aligned}
\sigma_f(\phi_\Gamma, T) &= \sigma_u(\phi_\Gamma) - T\sigma_s(\phi_\Gamma) \\
&= [\gamma_u(\phi_\Gamma) - T\gamma_s(\phi_\Gamma)] - [\gamma_u'(\phi_\Gamma) - T\gamma_s'(\phi_\Gamma)]\phi_\Gamma \\
&= \gamma_f(\phi_\Gamma, T) - \frac{\partial\gamma_f(\phi_\Gamma, T)}{\partial\phi_\Gamma}\phi_\Gamma.
\end{aligned}
\tag{C3}
$$

With the help of the definitions (A12), (B4), (B8), and (C3) and the following:

$$
\frac{\partial\gamma_f(\phi_\Gamma, T)}{\partial\phi_\Gamma} = \gamma_u'(\phi_\Gamma) - T\gamma_s'(\phi_\Gamma),
\tag{C4}
$$

$$
\lambda_f = \lambda_u - T\lambda_s = \eta[\sigma_f(\phi_\Gamma, T) - \sigma_0]\mu_0 - \eta\epsilon\frac{\partial\sigma_f}{\partial\phi_\Gamma}\boldsymbol{\nabla}\phi_\Gamma\cdot\boldsymbol{\nabla} c,
\tag{C5}
$$

$$
\hat{u} - T\hat{s} = \delta\gamma_f(\phi_\Gamma, T) + f(T, \rho),
\tag{C6}
$$

we rewrite Eq. (C2) as

$$
\begin{aligned}
\int_{V(t)} S_{\text{gen}}\, dV &= \int_{V(t)} \frac{1}{T}[\mathbf{m} + \eta\epsilon\sigma_f(\phi_\Gamma)(\boldsymbol{\nabla} c \otimes \boldsymbol{\nabla} c) - \gamma_f(\phi_\Gamma, T)\delta\mathbf{I} - f(T, \rho)\mathbf{I}]{:}\boldsymbol{\nabla} \boldsymbol{v} \\
&\quad - \frac{1}{T}\boldsymbol{\nabla}\cdot\left[\boldsymbol{q}_E + \boldsymbol{q}_E^{nc} + \eta\epsilon\sigma_u(\phi_\Gamma)\frac{Dc}{Dt}\boldsymbol{\nabla} c\right] + \boldsymbol{\nabla}\cdot\left[\frac{\boldsymbol{q}_E}{T} + \boldsymbol{q}_S^{nc} + \eta\epsilon\sigma_s(\phi_\Gamma)\frac{Dc}{Dt}\boldsymbol{\nabla} c\right] \\
&\quad - \frac{1}{T}(\lambda_f + \eta\sigma_0\mu_0)\frac{Dc}{Dt} - \frac{1}{T}\frac{\partial\gamma_f}{\partial\phi_\Gamma}\frac{D(\delta\phi_\Gamma)}{Dt}\, dV.
\end{aligned}
\tag{C7}
$$

Substituting Eqs. (A5) and (B3) into (C7), we obtain

$$
\begin{aligned}
&\int_{V(t)} S_{\text{gen}}\, dV \\
&= \int_{V(t)} \frac{1}{T}[\mathbf{m} + \eta\epsilon\sigma_f(\phi_\Gamma, T)(\boldsymbol{\nabla} c \otimes \boldsymbol{\nabla} c) - \sigma_f(\phi_\Gamma, T)\delta\mathbf{I} + \tilde{p}\mathbf{I}]\boldsymbol{\nabla} \boldsymbol{v} - \frac{\delta}{T}\frac{\partial^2\gamma_f}{\partial\phi_\Gamma^2}\boldsymbol{\nabla}\phi_\Gamma\cdot\boldsymbol{q}_{\phi_\Gamma} \\
&\quad + \boldsymbol{\nabla}\cdot\left\{-\frac{\boldsymbol{q}_E^{nc}}{T} + \boldsymbol{q}_S^{nc} - \eta\epsilon\left[\frac{1}{T}\sigma_u(\phi_\Gamma) - \sigma_s(\phi_\Gamma)\right]\frac{Dc}{Dt}\boldsymbol{\nabla} c + \frac{1}{T}\eta\sigma_0\mu_0\boldsymbol{q}_C + \frac{\delta}{T}\frac{\partial\gamma_f}{\partial\phi_\Gamma}\boldsymbol{q}_{\phi_\Gamma}\right\} \\
&\quad + \left[\boldsymbol{q}_E + \boldsymbol{q}_E^{nc} + \eta\epsilon\sigma_u(\phi_\Gamma)\frac{Dc}{Dt}\boldsymbol{\nabla} c - \eta\sigma_0\mu_0\boldsymbol{q}_C - \delta\frac{\partial\gamma_f}{\partial\phi_\Gamma}\boldsymbol{q}_{\phi_\Gamma}\right]\cdot\boldsymbol{\nabla}\frac{1}{T} - \frac{1}{T}\boldsymbol{\nabla}(\eta\sigma_0\mu_0)\cdot\boldsymbol{q}_C\, dV,
\end{aligned}
\tag{C8}
$$

where we define

$$
\tilde{p} = \tilde{p}_2 + \left[\left(c - \frac{1}{\alpha}\right)\lambda_f + \eta\sigma_0\mu_0 c\right] = -f(T, \rho) + \delta\frac{\partial\gamma_f}{\partial\phi_\Gamma}\phi_\Gamma\left[\left(c - \frac{1}{\alpha}\right)\lambda_f + \eta\sigma_0\mu_0 c\right],
\tag{C9}
$$

$$
\tilde{p}_2 = -f(T, \rho) + \delta\frac{\partial\gamma_f}{\partial\phi_\Gamma}\phi_\Gamma.
\tag{C10}
$$

For the first term of (C8), we denote the general stress tensor by $\mathbf{m} = \mathbf{m}_0 + \boldsymbol{\tau}$, in which $\boldsymbol{\tau}$ is the deviatoric stress tensor with zero trace, and $\mathbf{m}_0$ is the unknown part to be defined later. Moreover, we define $\boldsymbol{Dv} = \nabla\boldsymbol{v} - (\nabla\cdot\boldsymbol{v})\mathbf{I}/3$ as the deviatoric part of $\nabla\boldsymbol{v}$ and substitute into the last term of Eq. (C8) to obtain

$$\frac{1}{T}[\mathbf{m} + \eta\epsilon\sigma_f(\phi_\Gamma, T)(\nabla c \otimes \nabla c) - \sigma_f(\phi_\Gamma, T)\delta\mathbf{I} + \tilde{p}\mathbf{I}]{:}\nabla\boldsymbol{v}$$

$$= \frac{1}{T}[\mathbf{m}_0 + \eta\epsilon\sigma_f(\phi_\Gamma, T)(\nabla c \otimes \nabla c) - \sigma_f(\phi_\Gamma, T)\delta\mathbf{I} + \tilde{p}\mathbf{I}]{:}\boldsymbol{Dv} + \frac{1}{T}\boldsymbol{\tau}{:}\nabla\boldsymbol{v}$$

$$- \frac{1}{3T}[\mathbf{m}_0 + \eta\epsilon\sigma_f(\phi_\Gamma, T)(\nabla c \otimes \nabla c) - \sigma_f(\phi_\Gamma, T)\delta\mathbf{I} + \tilde{p}\mathbf{I}]{:}\mathbf{I}\nabla\cdot\boldsymbol{v}$$

$$= \frac{1}{T}[\mathbf{m}_0 + \eta\epsilon\sigma_f(\phi_\Gamma, T)(\nabla c \otimes \nabla c) - \sigma_f(\phi_\Gamma, T)\delta\mathbf{I} + \tilde{p}\mathbf{I}]{:}\boldsymbol{Dv} + \frac{1}{T}\boldsymbol{\tau}{:}\nabla\boldsymbol{v}$$

$$- \frac{1}{3T}[\mathrm{tr}\,\mathbf{m}_0 + \eta\epsilon\sigma_f(\phi_\Gamma, T)|\nabla c|^2 - 3\sigma_f(\phi_\Gamma, T)\delta + 3\tilde{p}]\nabla\cdot\boldsymbol{v}. \tag{C11}$$

Defining the pressure p by

$$-p = \tfrac{1}{3}\mathrm{tr}\,\mathbf{m} = -\tfrac{1}{3}[\mathrm{tr}\,\mathbf{m}_0 + \eta\epsilon\sigma_f(\phi_\Gamma, T)|\nabla c|^2 - 3\sigma_f(\phi_\Gamma, T)\delta + 3\tilde{p}], \tag{C12}$$

such that

$$-p\mathbf{I} = \mathbf{m}_0 + \eta\epsilon\sigma_f(\phi_\Gamma, T)(\nabla c \otimes \nabla c) - \sigma_f(\phi_\Gamma, T)\delta\mathbf{I} + \tilde{p}\mathbf{I}, \tag{C13}$$

$$\mathbf{m} = -p\mathbf{I} - \eta\epsilon\sigma_f(\phi_\Gamma, T)(\nabla c \otimes \nabla c) + \sigma_f(\phi_\Gamma, T)\delta\mathbf{I} - \tilde{p}\mathbf{I} + \boldsymbol{\tau}. \tag{C14}$$

By applying the identity (B3), Eq. (C11) can be further rewritten as

$$\frac{1}{T}[\mathbf{m} + \eta\epsilon\sigma_f(\phi_\Gamma, T)(\nabla c \otimes \nabla c) - \sigma_f(\phi_\Gamma, T)\delta\mathbf{I} + \tilde{p}\mathbf{I}]{:}\nabla\boldsymbol{v}$$

$$= \frac{1}{T}[\mathbf{m}_0 + \boldsymbol{\tau} + \eta\epsilon\sigma_f(\phi_\Gamma, T)(\nabla c \otimes \nabla c) - \sigma_f(\phi_\Gamma, T)\delta\mathbf{I} + \tilde{p}\mathbf{I}]{:}\nabla\boldsymbol{v}$$

$$= \frac{1}{T}p\mathbf{I} : \boldsymbol{Dv} + \frac{1}{T}\boldsymbol{\tau}{:}\nabla\boldsymbol{v} - \frac{1}{T}p\nabla\cdot\boldsymbol{v}$$

$$= \frac{1}{T}\boldsymbol{\tau}{:}\nabla\boldsymbol{v} + \frac{1}{T}\alpha p\nabla\cdot\boldsymbol{q}_C$$

$$= \frac{1}{T}\boldsymbol{\tau}{:}\nabla\boldsymbol{v} + \nabla\cdot\left(\frac{1}{T}\alpha p\boldsymbol{q}_C\right) - \frac{1}{T}\boldsymbol{q}_C\cdot\nabla(\alpha p) - \alpha p\boldsymbol{q}_C\cdot\nabla\frac{1}{T}. \tag{C15}$$

Substituting Eq. (C15) into Eq. (C8), we obtain the entropy generation (A27)

$$\int_{V(t)} S_{\mathrm{gen}}\,dV = \int_{V(t)} \nabla\cdot\left[-\frac{1}{T}\left(\boldsymbol{q}_E^{nc} - f_E^{nc}\right) + \boldsymbol{q}_S^{nc} + \eta\epsilon\sigma_s(\phi_\Gamma)\frac{Dc}{Dt}\nabla c\right] + \left(\boldsymbol{q}_E^{nc} - f_E^{nc}\right)\cdot\nabla\frac{1}{T}$$

$$+ \frac{1}{T}\boldsymbol{\tau} : \nabla\boldsymbol{v} - \frac{1}{T}\nabla\mu_c\cdot\boldsymbol{q}_C + \nabla\frac{1}{T}\cdot\boldsymbol{q}_E - \frac{\delta}{T}\frac{\partial^2\gamma_f}{\partial\phi_\Gamma^2}\nabla\phi_\Gamma\cdot\mathbf{P}\cdot\boldsymbol{q}_{\phi_\Gamma}\,dV, \tag{C16}$$

where we define

$$f_E^{nc} = -\eta\epsilon\sigma_u(\phi_\Gamma)\frac{Dc}{Dt}\nabla c + \mu_c\boldsymbol{q}_C + \delta\frac{\partial\gamma_f}{\partial\phi_\Gamma}\mathbf{P}\cdot\boldsymbol{q}_{\phi_\Gamma}, \tag{C17}$$

$$\mu_c = \eta\sigma_0\mu_0 + \alpha p. \tag{C18}$$

2. Specification of the fluxes

To ensure $S_{\text{gen}} \geqslant 0$ in Eq. (C16), we specify all the unknowns, $\boldsymbol{q}_C$, $\boldsymbol{q}_E$, $\boldsymbol{q}_E^{nc}$, and $\boldsymbol{q}_S^{nc}$ as the following:

$$\boldsymbol{q}_C = -m_c \nabla \mu_c, \tag{C19}$$

$$\boldsymbol{q}_E = -k \nabla (T - T_0), \tag{C20}$$

$$\boldsymbol{q}_E^{nc} = -\eta \epsilon \sigma_u(\phi_\Gamma) \frac{Dc}{Dt} \nabla c + \mu_c \boldsymbol{q}_C + \frac{\partial \gamma_f}{\partial \phi_\Gamma} \delta \boldsymbol{q}_{\phi_\Gamma}, \tag{C21}$$

$$\boldsymbol{q}_S^{nc} = -\eta \epsilon \sigma_s(\phi_\Gamma) \frac{Dc}{Dt} \nabla c, \tag{C22}$$

$$\mathbf{m} = -p\mathbf{I} - \eta \epsilon \sigma_f(\phi_\Gamma, T)(\nabla c \otimes \nabla c) + \sigma_f(\phi_\Gamma, T) \delta \mathbf{I} - \tilde{p}\mathbf{I} + \boldsymbol{\tau}, \tag{C23}$$

$$\boldsymbol{\tau} = \mu(\nabla \boldsymbol{v} + \nabla \boldsymbol{v}^T) - \frac{2}{3} \mu(\nabla \cdot \boldsymbol{v})\mathbf{I}, \tag{C24}$$

$$\boldsymbol{q}_{\phi_\Gamma} = -m_{\phi_\Gamma} \nabla \phi_\Gamma, \tag{C25}$$

where m_c is the degenerate mobility for the phase field function, μ_C is the chemical potential, $\tilde{p}$ is given in (C9), and k is the heat conduction coefficient. The surfactant flux $\boldsymbol{q}_{\phi_\Gamma}$ is obtained by using the following properties obtained from Eq. (A15):

$$\frac{\partial \gamma_f(\phi_\Gamma, T)}{\partial \phi_\Gamma} = \mu_\lambda + RT \ln \frac{\phi_\Gamma}{\phi_\Gamma^\infty - \phi_\Gamma}, \qquad \frac{\partial^2 \gamma_f(\phi_\Gamma, T)}{\partial \phi_\Gamma^2} = RT \frac{\phi_\Gamma^\infty}{\phi_\Gamma(\phi_\Gamma^\infty - \phi_\Gamma)} > 0, \tag{C26}$$

where m_{ϕ_Γ} is the diffusion coefficient. This gives Fick's law for diffusion flux.

Substituting the above unknown terms into Eq. (C16), we obtain the nonnegativity of the entropy generation (A28). In addition, substituting the above unknown terms into Eq. (A25) leads to the energy equation (A33), where the term h_s is defined as

$$h_s = [\mathbf{m} + \eta \epsilon \sigma_u(\phi_\Gamma)(\nabla c \otimes \nabla c) - u^{nc}\mathbf{I}] {:} \nabla \boldsymbol{v} - \nabla \cdot \left[\boldsymbol{q}_E^{nc} + \eta \epsilon \sigma_u(\phi_\Gamma) \frac{Dc}{Dt} \nabla c \right]$$

$$- (\lambda_u + \eta \sigma_0 \mu_0) \frac{Dc}{Dt} - \gamma_u'(\phi_\Gamma) \frac{D(\delta \phi_\Gamma)}{Dt}. \tag{C27}$$

APPENDIX D: SPECIFICATION FOR UNKNOWN TERMS

Nondimensional fluxes

The terms that appeared in the nondimensional system equations (8)–(12) are given as

$$\tilde{p} = -\frac{1}{\text{Ec}} f(T, \rho) + \frac{1}{\text{We}} \delta \frac{\partial \gamma_f}{\partial \phi_\Gamma} \phi_\Gamma + \frac{\eta}{\text{We}} \mu_0 c + \left(c - \frac{1}{\alpha} \right) \lambda_f, \tag{D1}$$

$$\lambda_f = \frac{\eta}{\text{We}} (\sigma_f - 1) \mu_0 - \frac{\eta \epsilon}{\text{We}} \frac{\partial \sigma_f}{\partial \phi_\Gamma} \nabla \phi_\Gamma \cdot \nabla c, \tag{D2}$$

$$h_s = \left[\mathbf{m} + \frac{1}{\text{We}} \eta \epsilon \sigma_u(\phi_\Gamma)(\nabla c \otimes \nabla c) - u^{nc}\mathbf{I} \right] {:} \nabla \boldsymbol{v} - \left(\lambda_u + \frac{\eta}{\text{We}} \mu_0 \right) \frac{Dc}{Dt}$$

$$+ \nabla \cdot \left(\frac{1}{\text{Pe}_c} m_c \mu_c \nabla \mu_c + \frac{1}{\text{M}_\Gamma \text{Pe}_\Gamma} \delta \frac{\partial \gamma_f}{\partial \phi_\Gamma} \mathbf{P} \cdot \nabla \phi_\Gamma \right) - \frac{1}{\text{M}_\Gamma} \gamma_u'(\phi_\Gamma) \frac{D(\delta \phi_\Gamma)}{Dt}, \tag{D3}$$

$$\lambda_u = \frac{\eta}{\text{We}} [\sigma_u(\phi_\Gamma) - \sigma_0] \mu_0 - \frac{\eta \epsilon}{\text{We}} \nabla \sigma_u(\phi_\Gamma) \cdot \nabla c. \tag{D4}$$

[1] H. Liu and M. Altan, Science and engineering of droplets: Fundamentals and applications, Appl. Mech. Rev. **55**, B16 (2002).

[2] Y. Zhu and Q. Fang, Analytical detection techniques for droplet microfluidics—A review, Anal. Chim. Acta **787**, 24 (2013).

[3] S. Abalde-Cela, P. Taladriz-Blanco, M. G. de Oliveira, and C. Abell, Droplet microfluidics for the highly controlled synthesis of branched gold nanoparticles, Sci. Rep. **8**, 2440 (2018).

[4] A. Li, H. Li, Z. Li, Z. Zhao, K. Li, M. Li Y. Song, Programmable droplet manipulation by a magnetic-actuated robot, Sci. Adv. **6**, eaay5808 (2020).

[5] D. J. Collins, A. Neild, A. deMello, A.-Q. Liu, and Y. Ai, The poisson distribution and beyond: Methods for microfluidic droplet production and single cell encapsulation, Lab Chip **15**, 3439 (2015).

[6] S. Haber and G. Hetsroni, The dynamics of a deformable drop suspended in an unbounded Stokes flow, J. Fluid Mech. **49**, 257 (1971).

[7] R. Balasubramaniam, C. E. Lacy, G. Woniak, and R. S. Subramanian, Thermocapillary migration of bubbles and drops at moderate values of the Marangoni number in reduced gravity, Phys. Fluids **8**, 872 (1996).

[8] J.-C. Xie, H. Lin, P. Zhang, F. Liu, and W.-R. Hu, Experimental investigation on thermocapillary drop migration at large Marangoni number in reduced gravity, J. Colloid Interface Sci. **285**, 737 (2005).

[9] M. Nallani and R. Subramanian, Migration of methanol drops in a vertical temperature gradient in a silicone oil, J. Colloid Interface Sci. **157**, 24 (1993).

[10] P. T. Brady, M. Herrmann, and J. M. Lopez, Confined thermocapillary motion of a three-dimensional deformable drop, Phys. Fluids **23**, 022101 (2011).

[11] Z. Yin, L. Chang, W. Hu, Q. Li, and H. Wang, Numerical simulations on thermocapillary migrations of nondeformable droplets with large Marangoni numbers, Phys. Fluids **24**, 092101 (2012).

[12] H. Liu, A. J. Valocchi, Y. Zhang, and Q. Kang, Lattice Boltzmann phase-field modeling of thermocapillary flows in a confined microchannel, J. Comput. Phys. **256**, 334 (2014).

[13] O. S. Pak, J. Feng, and H. A. Stone, Viscous Marangoni migration of a drop in a Poiseuille flow at low surface Péclet numbers, J. Fluid Mech. **753**, 535 (2014).

[14] N. Young, J. Goldstein, and M. J. Block, The motion of bubbles in a vertical temperature gradient, J. Fluid Mech. **6**, 350 (1959).

[15] M. K. Tripathi, K. Sahu, G. Karapetsas, K. Sefiane, and O. Matar, Non-isothermal bubble rise: Non-monotonic dependence of surface tension on temperature, J. Fluid Mech. **763**, 82 (2015).

[16] Z. Yin and Q. Li, Thermocapillary migration and interaction of drops: Two non-merging drops in an aligned arrangement, J. Fluid Mech. **766**, 436 (2015).

[17] S. Das, S. Mandal, and S. Chakraborty, Effect of transverse temperature gradient on the migration of a deformable droplet in a Poiseuille flow, J. Fluid Mech. **850**, 1142 (2018).

[18] A. Nadim, H. Haj-Hariri, and A. Borhan, Thermocapillary migration of slightly deformed droplets, Part. Sci. Technol. **8**, 191 (1990).

[19] L. Zhang and R. S. Subramanian, R. Balasubramaniam, Motion of a drop in a vertical temperature gradient at small Marangoni number—The critical role of inertia, J. Fluid Mech. **448**, 197 (2001).

[20] R. Balasubramaniam and R. S. Subramanian, Thermocapillary migration of a drop: An exact solution with Newtonian interfacial rheology and stretching/shrinkage of interfacial area elements for small Marangoni numbers, Ann. N.Y. Acad. Sci. **1027**, 303 (2004).

[21] M. Herrmann, J. M. Lopez, P. Brady, and M. Raessi, Thermocapillary motion of deformable drops and bubbles, in *Proceedings of the Summer Program, Stanford University, Center for Turbulence Research* (2008), p. 155.

[22] V. Sharanya and G. R. Sekhar, Thermocapillary migration of a spherical drop in an arbitrary transient Stokes flow, Phys. Fluids **27**, 063104 (2015).

[23] J.-C. Baret, Surfactants in droplet-based microfluidics, Lab Chip **12**, 422 (2012).

[24] Z. Y. Luo, X. L. Shang, and B. F. Bai, Effect of soluble surfactant on the motion of a confined droplet in a square microchannel, Phys. Fluids **31**, 117104 (2019).

[25] S. Guido and V. Preziosi, Droplet deformation under confined Poiseuille flow, Adv. Colloid Interface Sci. **161**, 89 (2010).

[26] S. Das, S. Mandal, and S. Chakraborty, Cross-stream migration of a surfactant-laden deformable droplet in a Poiseuille flow, Phys. Fluids **29**, 082004 (2017).

[27] R. Dandekar and A. M. Ardekani, Effect of interfacial viscosities on droplet migration at low surfactant concentrations, J. Fluid Mech. **902**, A2 (2020).

[28] S. Das, S. Mandal, S. Som, and S. Chakraborty, Migration of a surfactant-laden droplet in non-isothermal Poiseuille flow, Phys. Fluids **29**, 012002 (2017).

[29] S. Das, S. Mandal, and S. Chakraborty, Effect of temperature gradient on the cross-stream migration of a surfactant-laden droplet in Poiseuille flow, J. Fluid Mech. **835**, 170 (2018).

[30] V. Sharanya, G. P. R. Sekhar, and C. Rohde, Surfactant-induced migration of a spherical droplet in non-isothermal Stokes flow, Phys. Fluids **31**, 012110 (2019).

[31] X. Luo, Z. Y. Luo, and B. F. Bai, Effect of thermal convection on thermocapillary migration of a surfactant-laden droplet in a microchannel, Phys. Fluids **32**, 092009 (2020).

[32] C. Pozrikidis, Interfacial dynamics for Stokes flow, J. Comput. Phys. **169**, 250 (2001).

[33] C. Sorgentone and A.-K. Tornberg, A highly accurate boundary integral equation method for surfactant-laden drops in 3D, J. Comput. Phys. **360**, 167 (2018).

[34] C. Sorgentone and P. M. Vlahovska, Pairwise interactions of surfactant-covered drops in a uniform electric field, Phys. Rev. Fluids **6**, 053601 (2021).

[35] B. Dai and L. G. Leal, The mechanism of surfactant effects on drop coalescence, Phys. Fluids **20**, 040802 (2008).

[36] G. Tryggvason, B. Bunner, A. Esmaeeli, D. Juric, N. Al-Rawahi, W. Tauber, J. Han, S. Nas, and Y.-J. Jan, A front-tracking method for the computations of multiphase flow, J. Comput. Phys. **169**, 708 (2001).

[37] M. Muradoglu and G. Tryggvason, A front-tracking method for computation of interfacial flows with soluble surfactants, J. Comput. Phys. **227**, 2238 (2008).

[38] J. Zhang, D. M. Eckmann, and P. S. Ayyaswamy, A front tracking method for a deformable intravascular bubble in a tube with soluble surfactant transport, J. Comput. Phys. **214**, 366 (2006).

[39] R. Mittal and G. Iaccarino, Immersed boundary methods, Annu. Rev. Fluid Mech. **37**, 239 (2005).

[40] M.-C. Lai, Y.-H. Tseng, and H. Huang, An immersed boundary method for interfacial flows with insoluble surfactant, J. Comput. Phys. **227**, 7279 (2008).

[41] M.-C. Lai, Y.-H. Tseng, and H. Huang, Numerical simulation of moving contact lines with surfactant by immersed boundary method, Commun. Comput. Phys. **8**, 735 (2010).

[42] H. D. Ceniceros, The effects of surfactants on the formation and evolution of capillary waves, Phys. Fluids **15**, 245 (2003).

[43] Y.-C. Liao, E. I. Franses, and O. A. Basaran, Deformation and breakup of a stretching liquid bridge covered with an insoluble surfactant monolayer, Phys. Fluids **18**, 022101 (2006).

[44] Q. Xu, Y.-C. Liao, and O. A. Basaran, Can Surfactant Be Present at Pinch-Off of a Liquid Filament? Phys. Rev. Lett. **98**, 054503 (2007).

[45] M. Booty and M. Siegel, A hybrid numerical method for interfacial fluid flow with soluble surfactant, J. Comput. Phys. **229**, 3864 (2010).

[46] Z. Guo and P. Lin, A thermodynamically consistent phase-field model for two-phase flows with thermo-capillary effects, J. Fluid Mech. **766**, 226 (2015).

[47] S. Osher, R. Fedkiw, and K. Piechor, *Level Set Methods and Dynamic Implicit Surfaces* (Springer, New York, NY, 2004), Vol. 153.

[48] J.-J. Xu, Z. Li, J. Lowengrub, and H. Zhao, A level-set method for interfacial flows with surfactant, J. Comput. Phys. **212**, 590 (2006).

[49] J.-J. Xu, W. Shi, and M.-C. Lai, A level-set method for two-phase flows with soluble surfactant, J. Comput. Phys. **353**, 336 (2018).

[50] R. Scardovelli and S. Zaleski, Direct numerical simulation of free-surface and interfacial flow, Annu. Rev. Fluid Mech. **31**, 567 (1999).

[51] A. J. James and J. Lowengrub, A surfactant-conserving volume-of-fluid method for interfacial flows with insoluble surfactant, J. Comput. Phys. **201**, 685 (2004).

[52] A. Alke and D. Bothe, 3D numerical modeling of soluble surfactant at fluidic interfaces based on the volume-of-fluid method, Fluid Dyn. Mater. Proc. **5**, 345 (2009).

[53] E. Uzgoren, J. Sim, and W. Shyy, Marker-based, 3-D adaptive Cartesian grid method for multiphase flow around irregular geometries, in *46th AIAA Aerospace Sciences Meeting and Exhibit* (American Institute of Aeronautics and Astronautics, Reston, VA, 2009), p. 1239.

[54] S. Ganesan and L. Tobiska, Arbitrary Lagrangian–Eulerian finite-element method for computation of two-phase flows with soluble surfactants, J. Comput. Phys. **231**, 3685 (2012).

[55] Q. Zhao, W. Ren, and Z. Zhang, A thermodynamically consistent model and its conservative numerical approximation for moving contact lines with soluble surfactants, Comput. Methods Appl. Mech. Eng. **385**, 114033 (2021).

[56] J. Lowengrub and L. Truskinovsky, Quasi–incompressible Cahn–Hilliard fluids and topological transitions, Proc. R. Soc. London A **454**, 2617 (1998).

[57] J. Shen and X. Yang, A phase-field model and its numerical approximation for two-phase incompressible flows with different densities and viscosities, SIAM J. Sci. Comput. **32**, 1159 (2010).

[58] H. Liu and Y. Zhang, Phase-field modeling droplet dynamics with soluble surfactants, J. Comput. Phys. **229**, 9166 (2010).

[59] G. Soligo, A. Roccon, and A. Soldati, Coalescence of surfactant-laden drops by phase field method, J. Comput. Phys. **376**, 1292 (2019).

[60] G. Zhu, J. Kou, B. Yao, Y.-s. Wu, J. Yao, and S. Sun, Thermodynamically consistent modelling of two-phase flows with moving contact line and soluble surfactants, J. Fluid Mech. **879**, 327 (2019).

[61] K. E. Teigen, P. Song, J. Lowengrub, and A. Voigt, A diffuse-interface method for two-phase flows with soluble surfactants, J. Comput. Phys. **230**, 375 (2011).

[62] K. E. Teigen, X. Li, J. Lowengrub, F. Wang, and A. Voigt, A diffuse-interface approach for modeling transport, diffusion and adsorption/desorption of material quantities on a deformable interface, Commun. Math. Sci. **7**, 1009 (2009).

[63] X. Li, J. Lowengrub, A. Rätz, and A. Voigt, Solving PDEs in complex geometries: A diffuse domain approach, Commun. Math. Sci. **7**, 81 (2009).

[64] Z. Guo, F. Yu, P. Lin, S. Wise, and J. Lowengrub, A diffuse domain method for two-phase flows with large density ratio in complex geometries, J. Fluid Mech. **907**, A38 (2021).

[65] F. Yu, Z. Guo, and J. Lowengrub, Higher-order accurate diffuse-domain methods for partial differential equations with Dirichlet boundary conditions in complex, evolving geometries, J. Comput. Phys. **406**, 109174 (2020).

[66] C.-S. Yih, *Fluid Mechanics: A Concise Introduction to Theory* (West River Press, Ann Arbor, MI, 1979).

[67] Z. Guo, P. Lin, J. Lowengrub, and S. M. Wise, Mass conservative and energy stable finite difference methods for the quasi-incompressible Navier-Stokes-Cahn-Hilliard system: Primitive variable and projection-type schemes, Comput. Methods Appl. Mech. Eng. **326**, 144 (2017).

[68] W. Feng, Z. Guo, J. S. Lowengrub, and S. M. Wise, A mass-conservative adaptive fast multigrid solver for cell-centered finite difference methods on block-structured, locally-Cartesian grids, J. Comput. Phys. **352**, 463 (2018).

[69] Y. Wang and P. Dimitrakopoulos, Low-Reynolds-number droplet motion in a square microfluidic channel, Theor. Comput. Fluid Dyn. **26**, 361 (2012).

[70] J. Horwitz, P. Kumar, and S. Vanka, Three-dimensional deformation of a spherical droplet in a square duct flow at moderate Reynolds numbers, Int. J. Multiphase Flow **67**, 10 (2014).

[71] X. Shang, Z. Luo, E. Y. Gatapova, O. A. Kabov, and B. Bai, GNBC-based front-tracking method for the three-dimensional simulation of droplet motion on a solid surface, Comput. Fluids **172**, 181 (2018).

[72] P. Hadland, R. Balasubramaniam, G. Wozniak, and R. Subramanian, Thermocapillary migration of bubbles and drops at moderate to large Marangoni number and moderate Reynolds number in reduced gravity, Exp. Fluids **26**, 240 (1999).

[73] S. S. Kalichetty, T. Sundararajan, and A. Pattamatta, Thermocapillary migration and interaction dynamics of droplets in a constricted domain, Phys. Fluids **31**, 022106 (2019).

[74] H. Garcke, K. F. Lam, and B. Stinner, Diffuse interface modelling of soluble surfactants in two-phase flow, Commun. Math. Sci. **12**, 1475 (2013).

[75] P. A. Kralchevsky, K. D. Danov, and N. D. Denkov, Chemical physics of colloid systems and interfaces, *Handbook of Surface and Colloid Chemistry*, edited by K. S. Birdi, Handbook of Surface and Colloid Chemistry (CRC Press, New York, 2002), Chap. 5.

[76] J. Chen and K. J. Stebe, Surfactant-induced retardation of the thermocapillary migration of a droplet, J. Fluid Mech. **340**, 35 (1997).